

Review

Achievements and Prospects of Molecular Dynamics Simulations in Thermofluid Sciences

Yunmin Ran and Volfango Bertola * 

Laboratory of Technical Physics, University of Liverpool, Brownlow Hill, Liverpool L69 3GH, UK;
yunmin.ran@liverpool.ac.uk

* Correspondence: volfango.bertola@liverpool.ac.uk; Tel.: +44-151-794-4804

Abstract: In the last decades, molecular dynamics (MD) simulations established as an important tool for solving fluid flow and heat transfer problems at the nanoscale, with a significant perspective impact on a wide range of industrial and scientific applications. As usual, this happened with several scholarly papers on this topic being published in the same period. The present article provides a thorough review of molecular dynamics (MD) simulations in the domain of fluid flow and heat transfer. In the first section, a survey of the physical modelling of heat transfer phenomena by MD simulations is presented, focusing on bubble and droplet nucleation and interfacial thermal behaviours. Subsequently, MD simulations of fluid flow and heat transfer in nanochannels are discussed, including adiabatic flow, convective heat transfer, and two-phase flow. Particular emphasis was placed on critical phenomena such as evaporation and condensation, to assess the effects of confinement within nanochannels. Finally, some of the current and emerging challenges in MD simulations and suggests future research directions are discussed.

Keywords: molecular dynamics simulation; fluid flow; heat transfer



Citation: Ran, Y.; Bertola, V. Achievements and Prospects of Molecular Dynamics Simulations in Thermofluid Sciences. *Energies* **2024**, *17*, 888. <https://doi.org/10.3390/en17040888>

Academic Editors: Marzena Iwaniszyn and Mateusz Korpys

Received: 4 January 2024

Revised: 4 February 2024

Accepted: 12 February 2024

Published: 14 February 2024



Copyright: © 2024 by the authors. Licensee MDPI, Basel, Switzerland. This article is an open access article distributed under the terms and conditions of the Creative Commons Attribution (CC BY) license (<https://creativecommons.org/licenses/by/4.0/>).

1. Introduction

The increasing technology challenges posed by miniaturisation of integrated fluidic systems prompt a growing interest in the study of nanoscale fluid dynamics and heat transfer [1,2]. Common examples are the heat dissipation of electronic devices [3], water desalination [4], drug delivery [5], and devices used in life sciences [6,7]. Molecular Dynamics (MD) simulations are emerging as a powerful tool to improve the understanding of the physical mechanism of several phenomena in fluid mechanics, heat and mass transfer. Based on Newton's second law of dynamics, MD simulations follow a systematic algorithmic framework to replicate the dynamic behaviour of atoms and molecules within a given system. This process begins with the initialization of particle positions and velocities, establishing the initial state of the system [8]. Subsequently, by employing numerical integration techniques, the equations of motion are solved over discrete time steps. This enables the prediction of particle trajectories based on the intermolecular forces calculated from suitable intermolecular potential energy functions and the current system configuration [9]. At each iteration, the forces acting on each particle are recalculated, thereby updating their positions and velocities. This iterative loop, known as a MD time step, advances the simulation in time and enables the observation of dynamic changes within the system.

Periodic boundary conditions are often applied to mimic an effectively infinite system, ensuring that particles interact as if they were surrounded by identical copies of themselves in a periodic lattice [10]. Moreover, to regulate temperature and pressure, thermostat and barostat algorithms may be integrated into the simulation framework [11,12]. Throughout the simulation, trajectories depicting the movements of particles are recorded at regular intervals. These trajectories serve as a rich source of data for subsequent analyses, offering

insights into significant properties such as temperature fluctuations, pressure variations, energy distribution, and structural transformations over time [13].

Early applications of MD simulations initially focused on static properties, involving calculations of equations of state and phase diagrams. The first MD simulation was carried out by Alder and Wainwright [14] to analyse particles moving at constant velocity subject to perfectly elastic collisions. Following this landmark achievement, in 1960, Gibson et al. [15] achieved a breakthrough by simulating radiation damage in solid copper. Their methodology involved a Born-Mayer type of repulsive interaction coupled with a cohesive surface force, representing one of the earliest instances of a realistic simulation of condensed matter. In 1964, Rahman [16] further advanced the field with simulations of liquid argon, employing the well-known Lennard-Jones potential to compute the intermolecular force field. The calculated system properties, including the coefficient of self-diffusion, exhibited impressive agreement with experimental data, establishing a solid foundation for subsequent molecular dynamics research. At this point, it is worth to remark the key role played by the choice of an appropriate intermolecular potential on the accuracy of simulations. A widely acknowledged issue in MD simulations is the often poor accuracy of classical interatomic potentials (such as the Lennard-Jones potential), which prevents a truly predictive modeling. This issue is becoming increasingly pressing especially in modelling biomolecular systems, where empirical potentials are often used, while it is less relevant to modelling simple liquids and gases, where classical potentials are generally adequate.

Advances in computing power and algorithms have empowered MD simulations to investigate dynamic processes with unprecedented detail, which includes nanoscale fluid dynamics, interfacial heat transfer mechanisms, and phase change kinetics [10,17]. At present, molecular dynamics is outstanding among other *ab initio* methods, such as meso-scale Kinetic Monte Carlo (KMC) [18], Density Functional Theory (DFT) [19], or Many-Body Perturbation Theory (MBPT) [20]. These developments not only widen the use of molecular dynamics simulations in thermofluid sciences but also foster interdisciplinary collaboration, bridging molecular-level insights with macroscopic engineering principles [21].

The present review gives an overview of the recent literature about molecular dynamics (MD) simulations applied to thermofluid sciences. The principal reasons to investigate fluid flow and heat transfer in nanochannel by MD simulations instead of standard models based on the continuum approach, which are necessarily supplemented by constitutive models (such as Fourier's law), are the possibility to obtain a deeper physical insight of such constitutive models, and to validate them under the effects of confinement. Beginning with a detailed examination of the physical modelling of heat transfer phenomena, the review covers a number of different approaches to heat flux modelling, as well as to the analysis of interfacial phenomena carried out by MD simulations, encompassing critical aspects like velocity and thermal slip, and the issue of thermal resistance at the solid-liquid interface. In addition, the paper provides a thorough overview of MD simulations of phase change phenomena, including the complex processes of nucleation, boiling, evaporation, and condensation. Subsequently, the review shifts its focus on nanochannels, discussing both the adiabatic properties of single-phase flows, including velocity slip and wettability effects, and the behaviour of convective flows with heat exchange. After that, the review covers a number of studies on two-phase flows in nanochannels. Finally, the review addresses the main current challenges in the field, and outlines the most promising directions for future research.

2. Physical Modelling of Heat Transfer Phenomena in MD Simulations

The investigation of heat and mass transfer phenomena at molecular level is attracting a growing interest of the research community. This is driven by the need to improve our physical understanding of the fundamental mechanisms, which have an important role in applications to micro- and nanotechnologies. Understanding these physical mechanisms at the atomic and molecular scale holds the key to making breakthroughs in various fields,

ranging from advanced materials to state-of-the-art electronic devices. In addition, several emerging technologies, such as thin film fabrication in the semiconductor industry, nanotube manufacturing, characterization techniques, and the development of novel materials, are increasingly dependent on the accurate prediction of heat transfer behaviours at the nanometric scale [8,22,23].

Compared with traditional numerical simulation methods, MD simulations allow one to extend the analysis from the microscopic to the nanoscopic scale, including space (from micrometers down to nanometres), time (ranging from microseconds to picoseconds), and rate (involving extremely high heat fluxes on the order of gigawatts per meter square). Furthermore, MD simulations excel in modelling systems characterized by high complexity, including complicated geometries, heterogeneous materials, and multi-phase flows. This positions them as particularly well-suited for studying heat transfer in nanoscale systems, where conventional continuum-based models may prove inadequate [9,10,24,25]. Additionally, MD simulations have the flexibility to investigate a broad spectrum of operating conditions and environmental factors, providing invaluable insights for the design and optimization of heat exchangers, electronic devices, and various other thermal systems.

In the recent years, several detailed investigations into the fundamental mechanisms of heat transfer and fluid flows have been conducted by MD simulations, particularly phase change phenomena [26–38], which provided a deep understanding of interactions occurring at the nanoscale between liquids and solids. These involve phenomena such as wetting [39–43] and nucleation [44–48]. When it comes to three-phase interfaces, processes such as evaporation [28,33,36,49] condensation [34,50,51], or solidification [52–54] on a surface also were widely investigated. Notably, MD methods can be also combined with the conventional Navier-Stokes approaches in the context of multi-scale modelling [55–60]. This integration of methodologies is very promising in addressing complex heat and mass transfer phenomena across different scales.

In this section, we first present the fundamental equations that describe the evolution of a system in the MD approach, as well as the heat flux modelling in MD simulations, providing different methods to compute the heat flux and the thermal conductivity using MD. Subsequently, we shift our focus to the interface behavior, with particular emphasis on the calculation of the thermal resistance, which represents a significant mismatch between the macroscopic and microscopic scales. Finally, we review MD approaches to model phase change phenomena, including boiling, evaporation, and condensation.

2.1. Fundamentals of MD Approach

Modelling the heat flux at atomic/molecular level by means of MD simulations is of paramount importance to shed light on heat diffusion mechanisms, including the well-known paradoxes of macroscopic continuum models [61]. Various approaches, such as the Green-Kubo formalism [62], have been used to quantitatively compute the heat flux and the thermal conductivity [63]. By employing equilibrium MD simulations, accurate estimations of the thermal transport properties have been obtained in different media, including crystalline solids, amorphous systems, and liquids [64]. Additionally, non-equilibrium Molecular Dynamics (NEMD) methods, such as the direct and reverse NEMD methods, offer insights into transient heat conduction and ballistic thermal transport, providing a comprehensive picture of heat flux dynamics in MD simulations [65,66].

As previously mentioned, the application of Newton's second law in MD simulations is introduced through the gradient of the potential function, as illustrated in the formula below [26]:

$$F_i = \sum_{i \neq j} F_{ij} = m_i \frac{d^2 r_i}{dt^2} = m_i \frac{dv_i}{dt} \quad (1)$$

The position r_i and velocity v_i of atom i can be calculated by integrating Equation (1); from this information one can then extract the macroscopic quantities of the system, including thermodynamic quantities, through suitable ensemble averaging, as discussed below. The Newton equation is generally integrated using the velocity Verlet method [22]:

$$v(t + \frac{\Delta t}{2}) = v(t) + \frac{a(t)}{2} \Delta t \quad (2)$$

$$r(t + \Delta t) = r(t) + v(t + \frac{\Delta t}{2}) \Delta t \quad (3)$$

where $r(t)$ and $v(t)$ are the position and velocity at time t , respectively, and Δt is the time step, which is usually of the order of 10^{-12} s to 10^{-15} s to resolve accurately intramolecular fluctuations. The computation of temperature is carried out based on the Gaussian distribution, as expressed by the following equation:

$$\frac{1}{N_{atoms}} \sum_{i=1}^{N_{atoms}} \frac{1}{2} m v_i^2 = \frac{3}{2} k_B T \quad (4)$$

where N_{atoms} is the number of atoms in the group, k_B is the Boltzmann constant, and T is the thermodynamic temperature.

The interatomic or intermolecular forces are expressed as the gradient of suitable potential functions, the most common of which is the well-known Lennard-Jones potential, which can be expressed as [67–69]:

$$\phi(r) = 4\epsilon \left[\left(\frac{\sigma}{r} \right)^{12} - \left(\frac{\sigma}{r} \right)^6 \right] \quad (5)$$

where $\phi(r)$ represents the potential energy, ϵ is the depth of the potential energy well, σ is the finite distance at which the inter-particle potential is zero, and r is the distance between the atoms or molecules, as shown schematically in Figure 1.

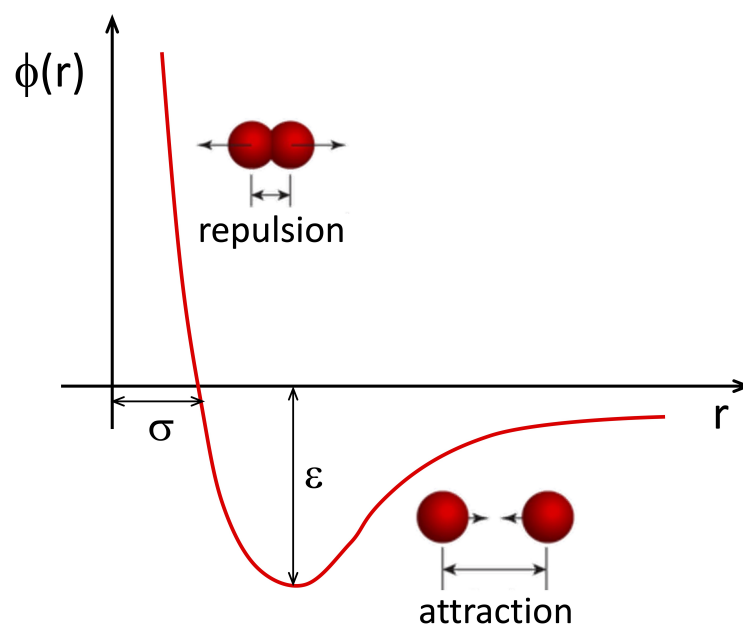


Figure 1. Schematic of the Lennard-Jones potential defining intermolecular interactions in MDS.

The Lennard-Jones (LJ) potential is commonly used in simulations with simple fluids such as argon, which is one of the most frequently studied fluids in MD simulations [70–75]. In the case of water, the most commonly used potential energy functions for describing water molecules and their interactions are based on simple pairwise additive functions with fixed point charges, such as the well-known TIPnP and SPC force fields [76].

When a solid-liquid interface is present (e.g., at solid boundaries), materials such as copper [73–75] or platinum [70–72] and some other metallic materials [77–79] are typically

chosen, due to their simple and regular molecular (atomic) structure as compared, for example, to polymer materials. In these scenarios, the interaction potential between the fluid and the solid is also described using the LJ potential, with the parameters determined by the Berthelot mixing rule [80],

$$\sigma_{ij} = \frac{\sigma_{ii} + \sigma_{jj}}{2} \quad (6a)$$

$$\epsilon_{ij} = \sqrt{\epsilon_{ii} \cdot \epsilon_{jj}} \quad (6b)$$

where ϵ_{ij} is the energy parameter for the interaction between particles of type i and j ; ϵ_{ii} is the energy parameter for interactions within particles of type i ; ϵ_{jj} is the energy parameter for interactions within particles of type j . Additionally, carbon nanotubes (CNTs) are frequently discussed as solid walls due to their exceptional heat transfer capabilities [81–83].

2.2. Heat Flux and Thermal Conductivity

In many works where heat conduction is evaluated by MD simulations, the heat flux averaged over a control volume is calculated based on the following equation or one of its equivalent forms [71,84–87]:

$$q = \frac{1}{2V} \left[\sum_i^N m_i v_i^2 \vec{v}_{i,z} + \sum_i^N \sum_{j \neq i}^N u_{ij} \vec{v}_{i,j} + \sum_i^N \sum_{j \neq i}^N (z_{ij} f_{ij}) \vec{v}_{i,j} \right] \quad (7)$$

where V is the volume of the simulation cell, i.e., $V = L_x L_y L_z$.

The thermal conductivity is obtained by integrating the heat current autocorrelation function through the Green- Kubo formula [62]:

$$\lambda = \frac{1}{3Vk_B T^2} \int_0^\infty \langle \vec{J}(0) \cdot \vec{J}(t) \rangle dt \quad (8)$$

where λ is the thermal conductivity, and $\vec{J}(t)$ is the heat current vector at time t .

Several works discussed the heat flux and thermal conductivity in MD simulations [26,29,35,42,74,88–91]. Ikeshoji and Hafskjold [85] conducted simulations of temperature gradients with periodic boundary conditions by non-equilibrium molecular dynamics simulations. Using a stacked layer structure, an analysis of a 128-particle Lennard-Jones liquid system revealed good agreement with the macroscopic theory of heat conduction, except in proximity to the hot and cold thermal reservoirs. The thermal conductivity for this 128-particle system was approximately 10% lower than the value reported in the literature based on molecular dynamics computations. In contrast, a run with a 1024-particle system demonstrated close alignment with the literature values, showing differences within a 1–2% range, which were attributed to statistical errors. Lukes et al. [29] used MD simulations to investigate the thermal conductivity in solid thin films perpendicular to the film plane. They observed an increase of conductivity with the film thickness, in agreement with experimental and theoretical predictions for thin films. Varying the boundary conditions, the heat flux and shape and size of the film causes no measurable changes in the thermal conductivity, although the calculated values exceed expectations by around 30%.

Tokumasu et al. [87] examined how molecular elongation affects the thermal conductivity in diatomic liquids using non-equilibrium molecular dynamics simulations. They used a two-center Lennard-Jones model to describe intermolecular interactions. The study found that increased molecular elongation led to a higher reduced thermal conductivity. They also found that the contribution of energy transport and translational energy transfer to heat flux is independent of the elongation of the molecules. However, the contribution to thermal conductivity arising from the rotational energy transfer increases with a greater molecular elongation.

Sun et al. [74] determined the thermal conductivity of an argon-based nanofluid containing copper nanoparticles under shear flow using molecular dynamics. They found

that in a Couette flow, the relative thermal conductivity is directly proportional to the shear rate due to enhanced “microconvection” caused by the rotation of nanoparticles. In addition, they found this effect is more prominent at lower nanoparticle volume fractions, which was attributed to slower rotation speeds.

2.3. Interface Behaviours in MD Simulations

2.3.1. Hydrodynamic and Thermal Wall Slip

In conventional macroscopic hydrodynamics, it is commonly assumed there is no slip between the fluid and the wall at solid boundaries. However, empirical observations at microscopic or smaller scales consistently exhibit slip flow [92–96]. These observations include discontinuous shear stresses, slip lengths comparable to the characteristic length of the system, non-Newtonian viscosity, and strong fluid ordering. While these factors may not be a primary concern at the macroscale, they have considerable importance at the nanoscale [3,97–99].

Studies on systems consisting of liquid films and solid walls [91,97,100–118] extensively examined the velocity distributions and the shear stresses near the solid-liquid interface for either Poiseuille or Couette flow of Lennard-Jones fluids. These studies revealed the effects of several parameters, including the number densities of either the solid or the liquid molecules [91,97,104,106,107], the intermolecular potential between solid and liquid molecules [97,100,104–108,108–110,113], the roughness of the solid surface [97,114,119], the gap between the solid walls [105], the molecular species constituting the liquid [110–112], and the pressure of the system [97]. In addition, several investigations specifically addressed the slip length, a critical parameter in understanding the interfacial behaviour between fluids and solid walls [120–123].

At the nanoscale, liquids exhibit near-wall density fluctuations, often referred to as molecular layering or adsorption layers, which are due to the influence of wall force fields [124,125]. These density fluctuations, displayed qualitatively in Figure 2a, have been extensively investigated [79,91,103,126–130], and MD simulations represent an ideal tool to study the fluid structure as well as the wall-fluid interactions at such small scales [131–134]. These simulations revealed that when a fluid adheres to a solid surface, it forms distinct layers. In the case of simple Lennard-Jones fluids sheared between parallel solid walls, the layering effect is typically noticeable up to a distance of about five molecular diameters from the solid-fluid interface [107,131,135,136]. Within this region, the fluid properties and the phase behavior deviate from the bulk fluid [109,131,135,137,138]. Beyond this distance, these structural effects progressively vanish, and the fluid properties approach their bulk values. Lautenschlaeger and Hasse [91] studied the effect of adsorption on the fluid properties by MD simulations. It was found that most fluid properties, including pressure p , density ρ , internal energy u , enthalpy h , the isobaric heat capacity c_p , the thermal expansion coefficient α_p , the thermal conductivity λ , the shear viscosity η , and the self-diffusion coefficient D , are affected by the solid-fluid interaction and the bulk temperature of the fluid. Schmitt et al. [139] investigated nanoscale heat transfer across a solid-fluid interface in a system consisting of a fluid confined between two parallel plane walls. They observed the multiple layers of particles in the adsorption film, which reaches a thickness of approximately eight times the size parameter of the Lennard-Jones potential, σ . In addition to molecular layering, other important nanoscale interfacial effects, particularly in regimes characterized by transition or free molecular flow, are the interfacial thermal resistance [70] and the capillary pumping process, which relies on meniscus deformation, and might weaken because of the disappearance of liquid meniscus structures at the nanoscale [140].

The thermal transport through the interface between two different materials results into a temperature jump (ΔT_i) at the fluid-solid interface, as displayed qualitatively in Figure 2b. This temperature jump is proportional to the heat flux (\vec{j}), through a thermal resistance known as the Kapitza resistance, (R_k):

$$\Delta T_i = -R_k \vec{j} \cdot \vec{n} \quad (9)$$

where \vec{n} is the outward unit normal from the wall. The Kapitza resistance is usually expressed in terms of the Kapitza length [141], which is analogous to the slip length in fluid dynamics.

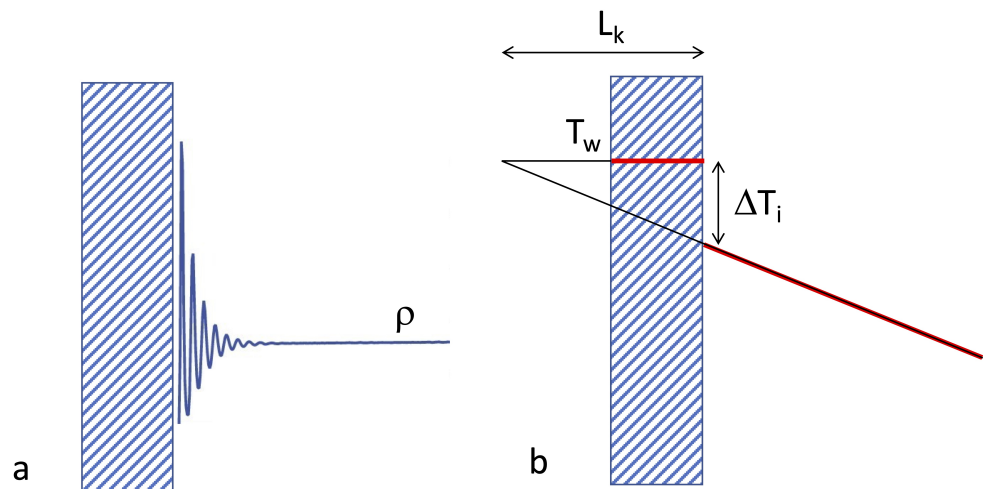


Figure 2. Typical density (a) and temperature profile (b) of a fluid near a solid wall. The discontinuity of temperature profile defines the interface thermal resistance, quantified by the Kapitza length, L_K .

The hydrodynamic slip length is defined as follows:

$$l_s = \frac{\Delta u_i}{\frac{\partial u}{\partial n}|_{\text{liquid}}} \quad (10)$$

where l_s is the slip length, Δu_i is the difference between the velocities of the fluid and the wall, also known as the slip velocity, and $\partial u / \partial n$ is the velocity gradient in the fluid.

Similar to the concept of slip length for velocity, one can define a “thermal resistance length”, denoted as l_k , which is also referred to as the Kapitza length. This length is determined by extrapolating the temperature profile within the liquid into the solid until the actual wall temperature is reached. The Kapitza length is formally defined as:

$$l_k = \frac{\Delta T_i}{\frac{\partial T}{\partial n}|_{\text{liquid}}} \quad (11)$$

where $\partial T / \partial n$ is the temperature gradient on the side of the liquid, and $\Delta T_i = T_{\text{fluid}} - T_{\text{wall}}$. It must be noted, however, that the definition of a thermal gradient requires the introduction of the continuum approximation, otherwise temperature and its derivatives cannot be defined.

Maruyama and Kimura [142] demonstrated that the interface thermal resistance and the temperature jump at solid-liquid interfaces are strongly influenced by wettability. They simulated a system consisting of an argon vapour region sandwiched between two argon liquid layers, both modelled using the Lennard-Jones potential, which were in contact with two platinum solid walls (where the heat conduction through free electrons was artificially neglected to make the material electrically insulating). Subsequent studies revealed a consistent decrease of the Kapitza length with increasing wettability [39,89,143–148]. Figure 3 displays the Kapitza resistance as a function of temperature, for different surface wettabilities, expressed in terms of the surface energy.

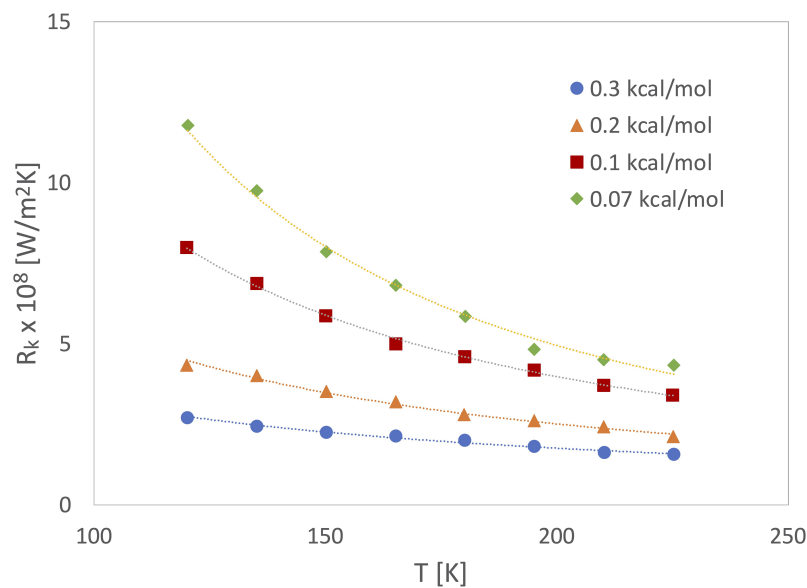


Figure 3. The Kapitza resistance as a function of temperature, for different magnitudes of the surface energy (the solid lines are fitted with the function form $R_K = R_0 T^{-\alpha}$). Data replotted from [145].

In addition to wettability, several other parameters affect both the hydrodynamic and the thermal slip at the nanoscale, including the channel width [149,150], the surface geometry [78,151], temperature [152–155], the fluid density [156,157], and the solid–solid interactions [141,158–160]. For example, Murad et al. [147,161] found that the Kapitza resistance decreases as a function of temperature, following a $T^{-\alpha}$ relationship, for both water–SiO₂ and water–Si interfaces, with a stronger dependence in the case of the water–SiO interface.

Barisik et al. [144] conducted a comprehensive investigation into the temperature dependence of thermal resistance at a water/silicon interface. They discussed three scenarios of water confined between two silicon walls, employing varying hot wall temperatures of 363 K, 353 K, and 343 K, and cold wall temperatures of 283 K, 292 K, and 303 K, respectively. Their simulations revealed a reduction in interfacial thermal resistance as temperature increased, particularly on a surface with favorable wettability. Through an examination of the liquid structure close to the solid, they attributed this decrease in resistance to a higher density of phonon states at elevated temperatures, leading to enhanced vibrational coupling. Kim et al. [88,143] investigated the thermal interactions in nanoscale fluid flow, performing a systematic study of the Kapitza length as a function of the relative surface wettability $\varepsilon_{wf}/\varepsilon$, and the thermal oscillation frequency, showing that the Kapitza length increases by increasing the thermal oscillation frequency and by decreasing the surface wettability.

2.3.2. Wetting on Solid–Liquid Interfaces

In addition to the slip and Kapitza lengths, the use of MD simulations to investigate interfacial phenomena includes the study of drop–surface interactions. In particular, the wetting behaviour can be characterised through either the true or the apparent contact angle, which can be inferred from the density contour of sessile drops using an image processing technique [162,163].

The equilibrium at the solid–liquid–vapour interface is ruled by the Young–Laplace equation:

$$\gamma_{SV} = \gamma_{SL} + \gamma_{LV} \cos \theta_{\infty} \quad (12)$$

where γ_{SV} , γ_{SL} , and γ_{LV} are the interfacial tensions between the solid and the vapour, the solid and the liquid, and the liquid and the vapour, respectively, while θ_{∞} is the equilibrium contact angle for a macroscopic droplet.

As the droplet size is reduced, the three-phase interactions at the liquid-solid-vapour contact line are no longer explained only in terms of the interfacial tensions between each pair of phases. In addition to these contributions, the line tension where these three interfaces converge becomes increasingly important. Thus, an additional energy per unit contact line length at the base of the droplet contributes to its free energy, resulting into a modification of the Young-Laplace equation [164]:

$$\gamma_{SV} = \gamma_{SL} + \gamma_{LV} \cos \theta_{\infty} + \frac{\tau}{r_B} \quad (13)$$

where τ is the line tension, and r_B is the droplet base radius, as shown schematically in Figure 4. Using Equations (12) and (13) can be written as:

$$\cos \theta = \cos \theta_{\infty} - \frac{\tau}{\gamma_{LV}} \frac{1}{r_B} \quad (14)$$

where $\cos \theta$ term is directly proportional to the droplet base contour line curvature $1/r_B$. In the limit of large droplets ($r_B \rightarrow \infty$), Equation (14) returns the Young-Laplace equilibrium contact angle, however, for droplets smaller than 100 nm the line tension effect cannot be neglected [165]. Thus, the microscopic contact angle differs from the macroscopic angle due to the influence of line tension. As the droplet size decreases, a positive line tension causes the droplet to contract, resulting in an increased contact angle. Conversely, a negative line tension promotes enhanced wetting.

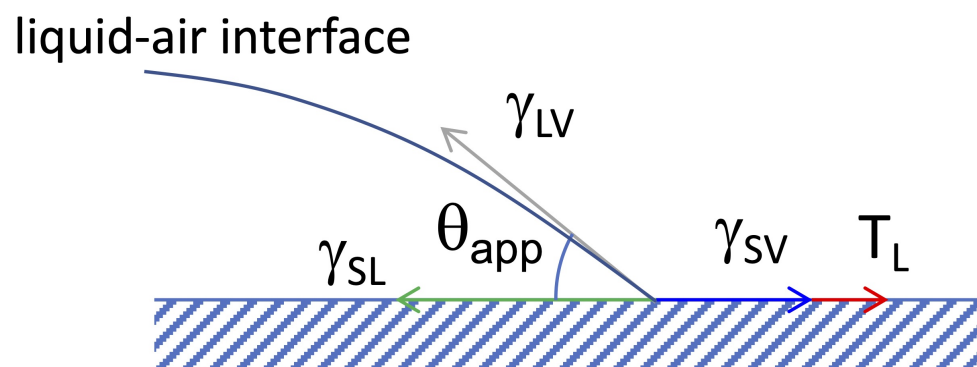


Figure 4. Schematic of interfacial forces acting on the three-phase (solid-liquid-gas) contact line formed by a liquid drop deposited on a solid surface, including the line tension, T_L .

Barisik and coworkers [144,156,166,167] made significant contributions to investigating the heat transfer mechanisms in solid-liquid systems. In particular, they conducted in-depth studies on the influence of wall temperature, pressure, and the contact angle of a droplet on the heat transfer mechanisms in water-silicon, water-gold, argon-graphite and argon-silver systems. Figure 5 shows the cosine of the contact angle as a function of the droplet base curvature $1/r_B$, for different wettabilities, obtained by changing the strength of intermolecular forces in the substrate, ϵ , with respect to its reference value, ϵ^* , under the assumption of a constant water surface tension of 72 mN/m. The slope of each linear fit is proportional to the line tension τ according to Equation (14). In case of low-energy surfaces the slope is negative, which means a positive line tension, while high-energy surfaces exhibit positive slopes and a negative line tension. By extrapolating the linear trends to large curvatures ($r_B \rightarrow \infty$, or $1/r_B \rightarrow 0$), one can predict the line tension magnitude for macroscopic drops [166]. The results of this procedure are in the range of experimental measurements of the line tension [168].

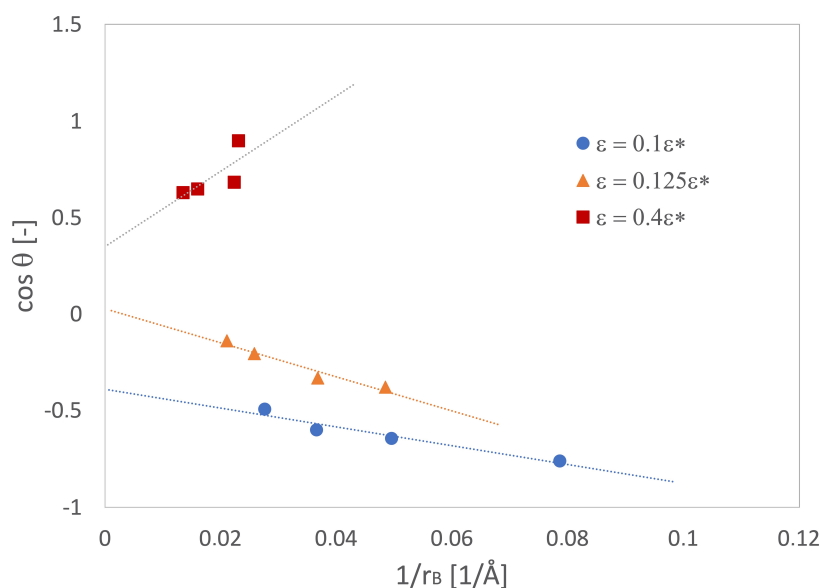


Figure 5. Cosine of the contact angle for droplets of different size as a function of the inverse of the droplet base radius, $1/r_B$, for different wettabilities of the surface. Dotted lines correspond to linear best fits. Contact angle data replotted from [166].

Ohara et al. [101,102] investigated the effect on interfacial heat transfer of crystal orientation, a factor linked to variations in the atom density within a solid. Goicochea et al. [169] and Acharya et al. [170] explored the effects of solid surface features such as functionalization, roughness, and composition. Lundgren et al. [171] reported that the contact angle of a liquid droplet deposited on a chemically heterogeneous surface aligns well with the Cassie-Baxter model when the drop size is significantly larger than the surface features. Halverson et al. [172], however, showed that the contact angle on certain chemically heterogeneous surfaces consisting of self-assembled monolayers does not conform to the Cassie-Baxter model, but rather to the Israelachvili-Gee model [173]. Wang et al. [174] further expanded the understanding, demonstrating that both positive and negative deviations from linear additivity of contact angles can be observed for aqueous nanodrops on heterogeneous synthetic (functionalised graphene) and natural (protein) surfaces. This nonlinear behaviour was attributed to the uneven exposure of the various mixture components to the solvent, which is a consequence of steric shielding when there is a significant difference in the polarity of the mixture components.

2.4. Phase Change Phenomena in MD Simulations

2.4.1. Bubble Nucleation and Boiling

Molecular dynamics enabled significant achievements in the understanding of phase change phenomena such as boiling and condensation. In the case of boiling, the classical theory of nucleation is the most widely used model to predict nucleation rates and critical cluster sizes, providing fundamental insights into the initiation of vapour bubble formation [175,176]. More recently, various theoretical approaches including the Density Functional Theory (DFT) [177,178], the Square Gradient Theory [179], and some modifications of the classical theory [180,181] have been used to describe the process of bubble nucleation. Measuring bubble nucleation rates proves to be a significant challenge in laboratory experiments. However, this can be achieved in a relatively straightforward way through computer simulations, and in particular molecular dynamics simulations.

The early MD simulations of bubble nucleation in general tend to exhibit discrepancies with respect to the classical nucleation theory. Zhukhovitskii [182] used MD simulation to investigate the growth and decay of single clusters within a supersaturated vapour. It was found that the critical nucleus size was larger than that predicted by the classical nucleation

theory. However, the estimation of the critical size of the nucleus using the classical nucleation theory requires experimental values of surface tension, liquid density and saturation vapour pressure as inputs, therefore the discrepancy may be due to uncertainties in these quantities.

Yasuoka and Matsumoto [183,184] conducted direct MD simulations of the nucleation process both for a Lennard-Jones liquid and for water. The nucleation rate, defined as the number of nuclei (larger than the critical nucleus) generated per unit time and per unit volume, was found to be seven orders of magnitude larger than the value predicted by the classical nucleation theory. Kinjo and Matsumoto [46] demonstrated the formation of a cavity in negative pressure using Lennard-Jones liquid, revealing a nucleation rate eight orders of magnitude larger than that predicted by classical nucleation theory. The large difference is attributed to a flaw in the theory, i.e., the persisting free energy barrier near the spinodal region.

In addition to homogeneous nucleation, heterogeneous nucleation is also discussed. Maruyama et al. [185] simulated the heterogeneous nucleation of an Argon vapour bubble on a solid platinum surface, measuring the apparent contact angle, which was achieved by placing liquid argon between two parallel platinum solid surfaces and pulling them apart until nucleation occurred. Additionally, they also investigated the heterogeneous nucleation of an argon liquid droplet on a solid surface modelled as a constant temperature heat bath using phantom molecules [186].

Wu [45] investigated bubble nucleation in a homogeneous Lennard-Jones liquid heated at a constant mean negative pressure. Nagayama and Cheng [37,187] used molecular dynamics simulations to study bubble nucleation confined in a nanochannel, and investigated the effects of interfacial wettability on the flow in a nanochannel. Yamamoto and Matsumoto [47] investigated the initial stages of nucleate boiling on an ideally smooth surface using a molecular dynamics simulation. They conducted experiments where the entire surface was heated at first, and then only one part of the surface was heated while the other was cooled. She et al. [188] used MD simulations to analyse bubble formation in liquid argon on a platinum surface with a cavity. Hens et al. [48] conducted molecular dynamics simulations to gain insights into the mechanism of bubble formation on a platinum substrate, with particular focus on the surface texture.

2.4.2. Evaporation

Another phase change process different from bubble nucleation, occurring on small clusters, is droplet evaporation. Unlike macroscopic droplets, for which the diameter scales as the square root of time during evaporation, microscopic droplets, known as Knudsen particles, exhibit different evaporation rate laws [189]. For argon, the evaporation rate is expressed as:

$$\frac{dr}{dt} = -36.4 \sqrt{\frac{T}{M}} \frac{n_g}{n_l} f(\text{Kn}) E\left(\frac{m}{s}\right) \quad (15)$$

where T , M , n_g , n_l , Kn , $f(\text{Kn})$, and E are the absolute temperature, the molecular weight, the number density of the gas, the number density of the liquid, the Knudsen number, the Knudsen correction, and the evaporation coefficient, respectively. The Knudsen correction function, $f(\text{Kn})$, is expressed as

$$f(\text{Kn}) = \frac{1.333}{\frac{1}{\text{Kn}} + \frac{1.333\text{Kn}+0.71}{1+\text{Kn}}} \quad (16)$$

where the Knudsen number is defined as the mean free path divided by the droplet radius.

In a pioneering work by Long et al. [28], droplet evaporation was investigated using a model comprising 2048 argon atoms. This system included a single droplet and the surrounding vapor, both modeled using the Lennard-Jones 12-6 potential. The droplet was heated by increasing the temperature of the vapour phase at the system boundaries. The computed evaporation rate aligned closely with the prediction of the Knudsen particle

theory, as shown in Figure 6. Later, Little [190] conducted simulations on the sub- and super-critical evaporation of nanometer-sized droplets. For droplets measuring 8 nm (consisting of 5587 atoms), the computed evaporation coefficient was within a 20 percent deviation from the macroscopic evaporation law [191], which is expressed as

$$\frac{dD^2}{dt} = -\beta_{eva} \quad (17)$$

where β_{eva} is the evaporation coefficient, and D is the droplet diameter.

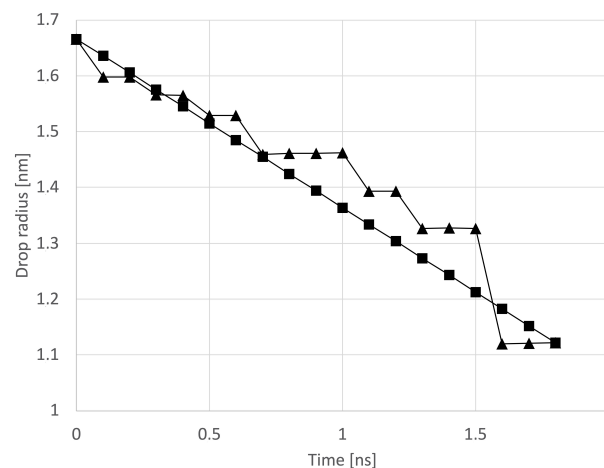


Figure 6. Comparison of the evaporation rate ($T = 120$ K; $P = 0.4$ MPa) of an argon droplet into argon gas from MD simulations (triangles) with theoretical predictions (squares). Theory data replotted from [189]; MD simulations replotted from [28].

Walther and Koumoutsakos [192] also compared with Equation (17) the subcritical evaporation of a nanometre-sized droplet at conditions of 300 K and 3 MPa. They integrated classical Molecular Dynamics techniques with an adaptive tree data structure to construct neighbour lists, enabling efficient simulations with hundreds of thousands of molecules. For the three different drop sizes considered (8 nm, 13 nm and 17 nm, respectively), the evaporation rate was found within 35% of the theoretical prediction for the smallest droplet, and less than 5% for the two larger droplets.

More recently, Consolini et al. [33] studied the subcritical and supercritical evaporation of xenon nanodroplets in a heated nitrogen atmosphere. In subcritical cases, initially nonspherical droplets quickly became spherical. In supercritical cases, the droplets maintained their non-spherical shape due to the absence of surface tension. Sumardiono and Fischer [49] investigated nano-droplet evaporation in vacuum. They observed that the system eventually reached equilibrium as predicted by the first law of thermodynamics. Gong et al. [193] studied the phase transition of droplets of a three-component hydrocarbon fuel (composed of 5.3 wt% isooctane, 25.8 wt% n-dodecane and 68.9 wt% n-hexadecane) in subcritical as well as supercritical nitrogen environments, and compared their results with the behaviour of single-component n-hexadecane droplets. Ju et al. [194] compared the evaporation rate of a single fuel droplet in both subcritical and supercritical environments, by means of experimental visualizations and molecular dynamics simulations. They found that in subcritical conditions, the evaporation rate of the droplet is inversely proportional to the density of droplet, therefore the evaporation rate first increases and then remains constant, which is in agreement with Equation (17).

In addition to droplet evaporation, there has been substantial research on film evaporation. Maroo and Chung [31,36] simulated a nanoscale evaporating meniscus consisting of a thin liquid argon film on a heated platinum surface. They studied the heat and mass transfer characteristics as well as pressure variation in the meniscus, and developed a novel thermal equilibrium model for the wall-fluid heat transfer boundary condition. Wu and

Pan [195] conducted a simulation of thin argon film evaporation on a platinum surface in vacuum. They derived the evaporation/condensation coefficient and observed that the mean temperature in the interface region was 2–3 K lower than that within the liquid. Yi et al. [196] investigated the evaporation of a thin layer of liquid argon on a platinum surface in the presence of an argon vapour atmosphere. The platinum surface was set at a constant temperature using the Langevin thermostat. The wall was then heated to the temperatures of 150 K and 300 K, respectively, starting from an initial equilibrium temperature of 110 K. Dou et al. [197] investigated the explosive boiling of water films adjacent to laser-irradiated hot surfaces.

2.4.3. Effects of Surface Roughness

Surface roughness and nano-structured surfaces have a significant influence on the phase change processes described above. Li et al. [198] were among the first to report an unexpected enhancement in boiling performance on nano-structured copper (Cu) surfaces compared to smooth surfaces. Several subsequent studies further explored the effects of various types of nano-structured surfaces on boiling enhancement [27,199–202]. Overall, the impact of micro/nano-surface structures on boiling heat transfer has been summarized by Kim et al. [203] as follows: (1) an increase in active nucleation site density due to randomly formed micro/nano-sized roughness; (2) the ability of vapour/gas entrapment to enhance cavities through re-entrant cavities fabrication and wettability control (resulting in an increase in liquid contact angle); (3) the promotion of favourable bubble initiation, growth, and departure on micro-porous layered surfaces; and (4) the enhancement of evaporation mass flux at the vapour-liquid interface facilitated by micro/nano structures.

2.4.4. Condensation

Similar to boiling or evaporation, during condensation nucleation and surface conditions are critical points that have been extensively investigated by molecular dynamics, although the literature on condensation is not as large as that on boiling and evaporation. Nagayama et al. [204] presented a theoretical derivation of the condensation coefficient based on the transition state theory, considering the three-dimensional movement of molecules in the liquid-vapour interface region. From a molecular scale perspective, it was observed that a characteristic length ratio plays a significant role in evaluating the condensation coefficient, with translational motion is more dominant than rotational motion in the condensation process. The MD results presented align closely with theoretical values for both monatomic and polyatomic polar molecules. Kesala et al. [205] conducted a study on the growth speed of nanoclusters during inert gas condensation on copper, silver, aluminum, and platinum. Their findings indicated that the condensation time is primarily influenced by the initial partial vapour pressure, as well as factors like molecular mass and lattice constant. Ranathunga et al. [206] conducted MD simulations to investigate water condensation on realistic surfaces of alkanethiol self-assembled monolayers featuring various head group chemistries. Their results demonstrated that reducing surface hydrophobicity leads to a notable increase in electrostatic forces between water molecules and the surface, consequently enhancing the rate of water condensation. This insight provides valuable information for understanding and controlling condensation processes on tailored surfaces. Wang et al. [207] investigated the density, heat capacity, and homogeneous condensation nucleation process of R1233zd, observing its transition from a superheated state to various supercooled states. They concluded that higher condensation pressure and lower condensation temperature were favorable factors for increasing the condensation rate.

In summary, molecular dynamics simulations have proven invaluable in understanding phase change phenomena, no matter whether heating or cooling. These simulations enable a detailed examination of atomic and molecular interactions at the interface between different phases. For instance, in boiling nucleation, MD simulations clarify the formation and growth of vapour bubbles. Similarly, in condensation nucleation, they shed light on the process of aggregation of vapour molecules to form droplets. Moreover, MD simulations

provide insights into evaporation, shedding light on the transition from liquid to vapour state. In addition, MD simulations have been instrumental in studying other phase change phenomena, such as freezing, melting, and sublimation. This computational approach facilitates a comprehensive understanding of the complex dynamics underlying phase transitions, offering important insights for a wide range of applications across physics, chemistry, materials science, and engineering.

3. Fluid Flow and Heat Transfer in Nanochannels by MD Simulations

The above section illustrated the fundamental phase change phenomena in various environments. In practice, nanoscale fluid flows usually occur in nanochannel geometries, where the effects of confinement may lead to significant differences with respect to macroscopic flows. In this section, first the behaviour of adiabatic flow at the nanoscale is discussed, examining how molecular interactions, surface roughness, and nanostructures influence the flow characteristics. Then, convective heat transfer in nanochannels is introduced. Finally, some works related to multi-phase flows confined in nanochannels are presented.

3.1. Adiabatic Flow in Nanochannels

Adiabatic flow, where there is no exchange of heat with the surroundings, is a fundamental phenomenon with wide-ranging applications in nanotechnology. Understanding the transport of liquids within nanoscale confinements is of much significance for various applications, such as water filtration and desalination [208], modelling fluid flow in shale reservoirs [209], and investigating drug transport across biological cell membranes [210]. Due to the dominant influence of the large surface area-to-volume ratio, fluids in nanoscale confinements experience distinctive wall force field effects, leading to markedly different behaviours compared to macroscale systems. Hence, a thorough understanding of nanoscale transport phenomena is necessary, and MD simulations serve as a powerful approach for such investigations. In particular, the dynamics of phase interfaces, flow patterns, and the effects of surface wettability on phase separation can be thoroughly examined by MD simulations.

The Poiseuille flow, being the most straightforward pressure-driven model, is widely used to analyse confined fluid flow within nanochannels. Travis et al. [211,212] conducted the nonequilibrium molecular dynamics (NEMD) simulations of a simple fluid undergoing planar Poiseuille flow in a nanochannel. They compared the simulation results against the predictions of classical Navier-Stokes theory for different channel widths, and found that the theory breaks down for very narrow pores. Figure 7 shows their result of streaming velocities with different channel sizes. For a channel width of 5.1 molecular diameters, the velocity profile deviates significantly from the Navier-Stokes hydrodynamic prediction. Conversely, at a channel width of 10.2 molecular diameters, classical Navier-Stokes behaviour is closely approximated.

To fully define the streaming velocity, they assumed no-slip boundary conditions, meaning that the tangential component of the velocity becomes zero at the boundary. However, in some cases, it has been observed that the tangential component of the streaming velocity is not exactly zero. Koplik and Banavar referred to this occurrence as ‘microscopic slip’ [213], although they also noted it is perfectly negligible at a macroscopic level. In many different studies, either no-slip, or slip, or liquid adsorption were observed at the liquid-wall interface [56,100,123,214], depending on the liquid-wall interaction strength. Nagayama and Cheng [187] conducted NEMD simulations to explore how the interface wettability influences the pressure-driven flow of a LJ fluid in a nanochannel. Their findings indicate that the hydrodynamic boundary condition at the solid-liquid interface is determined by the interface wettability. Figure 8 shows the velocity profiles of pressure driven flows with different interface wettability, where α is the potential energy factor indicating the strength of hydrophilic interaction, and β is the potential energy factor indicating the attraction for hydrophobic interaction. It is clear that, in a nanochannel

with hydrophilic surfaces, the velocity profiles exhibit the conventional parabolic shape. However, if the driving force surpasses a critical threshold, the no-slip boundary condition may become ineffective due to the interfacial resistance being overcome. In such instances, MD results show an adsorbed molecular layer sliding along the solid wall. Conversely, in a nanochannel with hydrophobic walls, a distinct gap forms between the liquid and the surface, resulting in minimal frictional resistance. This leads to a plug flow profile, and the slip length is dependent on the applied driving force. Moreover, it is noteworthy that non-uniform temperature and pressure profiles near the solid walls arise as a consequence of the interface wettability.

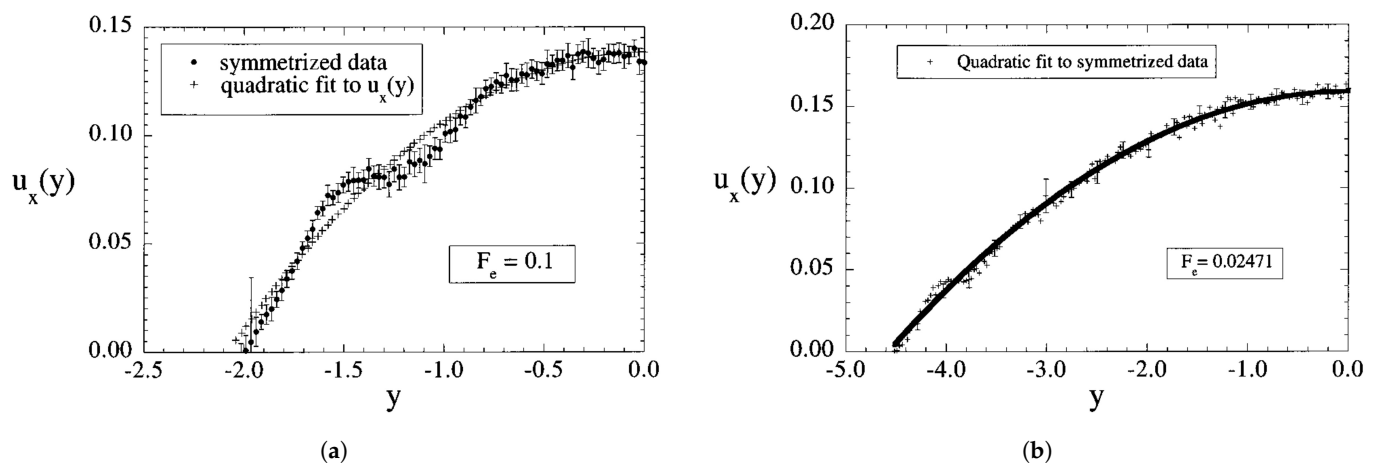


Figure 7. Streaming velocity profiles in channels with dimensionless width $W/\sigma = 5.1$ (a) and $W/\sigma = 10.2$ (b), where σ is the length constant of the WCA inter-atomic potential. Quadratic least-squares fits are overlaid on the data. Reprinted from [211] with permission.

Ghorbanian and Beskok [79] studied the force-driven liquid argon flows in nanoscale periodic domains and in gold nano-channels. Variations in the liquid density, viscosity, velocity profile, slip length, shear stress and mass flow rate in periodic domains of different size and nanochannels at a fixed thermodynamic state are discussed. The results show that liquid argon obeys to Newton's law of viscosity in the absence of walls, exhibiting the expected absolute viscosity even in domains as compact as four molecular diameters in height. This indicates that deviations from continuum solutions are exclusively attributed to wall effects. Thomas et al. [81] studied the pressure-driven water flow through carbon nanotubes (CNTs). Results are compared with experimental flow rate measurements through CNTs of similar size as well as through larger carbon nano pipes, and show that the flow through CNTs with diameters as small as 1.66 nm can be fully understood using continuum fluid mechanics.

Other simulations of force-driven liquid flows have demonstrated that density profiles in nanochannels remain unaffected by the magnitude of the driving force [211,215]. However, it is important to note that nano-confinements can lead to significant changes in liquid viscosity. The MD results suggested that viscosity is influenced by the distribution of the liquid near the wall as well as the structure of the wall [82,215].

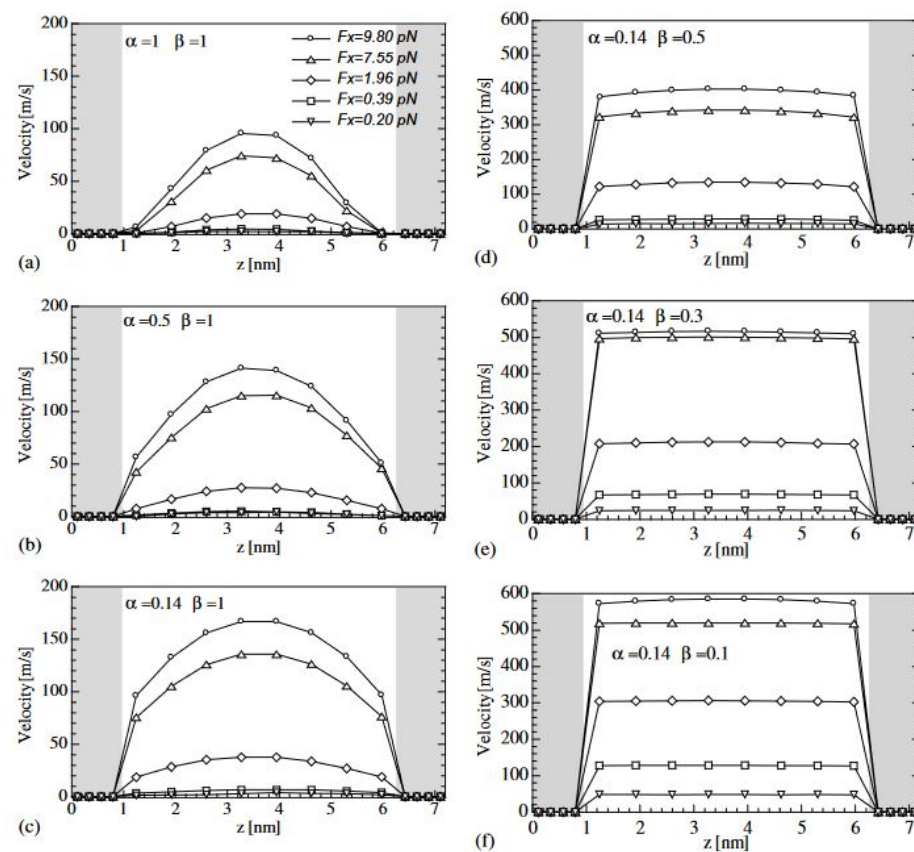


Figure 8. Velocity profiles in the z -direction of the pressure driven flow with different interface wettability. The parameter α indicates the strength of hydrophilic interaction, and β that of hydrophobic interaction. (a) $\alpha = 1$; $\beta = 1$. (b) $\alpha = 0.5$; $\beta = 1$. (c) $\alpha = 0.14$; $\beta = 1$. (d) $\alpha = 0.14$; $\beta = 0.5$. (e) $\alpha = 0.14$; $\beta = 0.3$. (f) $\alpha = 0.14$; $\beta = 0.1$. Reprinted from [187] with permission.

3.2. Convective Heat Transfer in Nanochannels

Convective heat transfer (both natural and forced) in nanochannels can be thoroughly examined using Molecular Dynamics (MD) simulations. In forced convective heat transfer, external forces drive the fluid flow, resulting into enhanced thermal transport. MD simulations enable detailed investigations into heat transfer coefficients, temperature profiles, and the effects of surface patterning on heat transfer enhancement. In scenarios where external forces (except buoyancy) are negligible, natural convection becomes a dominant heat transfer mechanism. MD simulations provide a platform to explore the impacts of temperature gradients and fluid properties on heat transfer rates.

At the macroscale, convective heat transfer relies on the no-slip boundary condition, where fluid velocity at the wall matches the wall velocity, as postulated by Stokes in 1851 [216]. However, at much smaller scales, particularly in the nanoscale, numerous studies have consistently demonstrated that this no-slip boundary condition doesn't hold in liquids. Instead, surface effects become dominant, leading to slip flow phenomena, as described above.

Furthermore, as dimensions scale down to the micro- and nanoscale, the convective heat transfer process, characterized by the dimensionless Nusselt number, Nu , diverges from the continuum theory. This observation has been corroborated by multiple reports [89,217–221]. The existence of a temperature discontinuity (temperature jump) at the wall, resulting from the Kapitza interfacial thermal resistance, leads to a reduction in interfacial fluid temperature gradients, which is mentioned previously. This ultimately causes deviations in the convective behaviour from what is conventionally observed in the macroscale [89,221–224]. The influence of these microscopic mechanisms varies depending

on factors such as the wall wettability, the geometric dimensions, the flow velocity, and the wall temperature.

Marable et al. [225] studied the convective heat transfer problem for a laminar flow of liquid water in graphene nanochannels under different test conditions by varying the strength of the graphene-water interaction, the channel height, the velocity of the fluid, and the wall temperature. Both hydrodynamic slip and thermal slip were observed, as shown in Figure 9. This figure illustrates the deviation from the no-slip boundary condition with respect to different parameters, by displaying both the hydrodynamic (l_s) and the thermal (or Kapitza) slip length (l_k) at the interface, with respect to the interaction strength, ϵ_{c-o} , the channel height, H , the mean velocity, $u_{f,avg}$, and the wall temperature, T_w . The influence of thermal slip was found to dominate over that of hydrodynamic slip since surface advection is not significant in environments characterised by high heat fluxes.

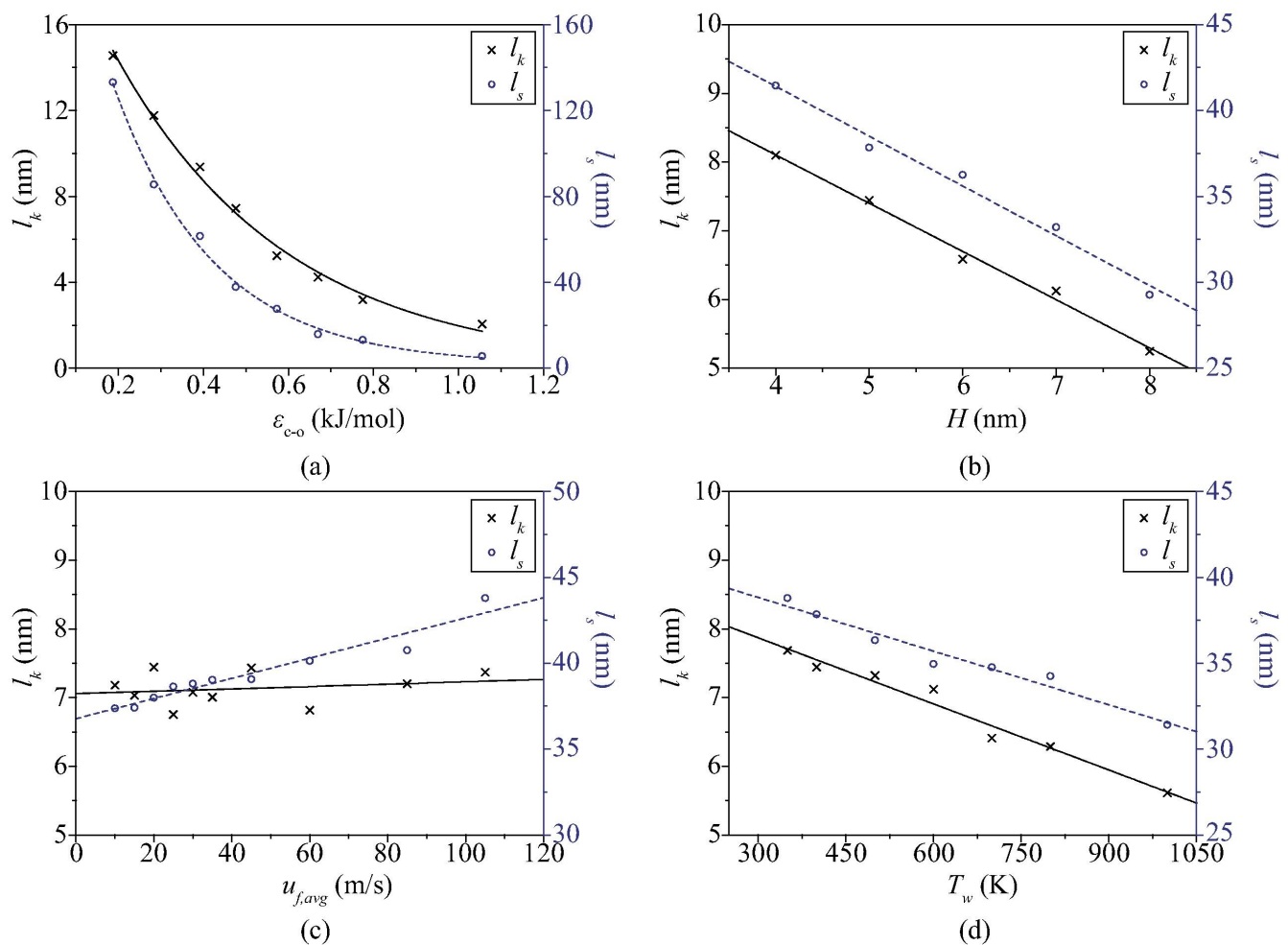


Figure 9. Thermal (l_k) and hydrodynamic (l_s) slip lengths as a function of (a) interaction strengths (ϵ_{c-o}), (b) channel heights (H), (c) velocities ($u_{f,avg}$), and (d) wall temperatures (T_w). Reprinted from [225] with permission.

The local heat transfer coefficient, denoted as $h(x)$, is defined as:

$$h(x) = \frac{q_s''(x)}{T_w - T_m(x)} \quad (18)$$

where $q_s''(x)$ is the local heat flux through the channel wall, T_w the temperature of the wall, and $T_m(x)$ denotes the local mean temperature at position x , which can be expressed as:

$$T_m(x) = \frac{\int_0^H c\rho(z)u_{f,x}(z)T(x,z)dz}{\int_0^H c\rho(z)u_{f,x}(z)dz} \quad (19)$$

where H is the height of the channel, c is the specific heat capacity, assumed to be constant, ρ is the density of the fluid, $u_{f,x}(z)$ is the fluid velocity in the x -direction, and $T(x,z)$ is the temperature of the fluid along the x -axis. Using the local kinetic energy and average velocity obtained from Molecular Dynamics simulations enables the calculation of $u_{f,x}(z)$ and $T(x,z)$.

The heat flux through the channel surface can be calculated as [10]:

$$q_s''(x) = \frac{Q}{A_s \Delta t} = \frac{1}{V} \left\{ \sum_i e_i u_{i,z} + \sum_{i < j} (\vec{f}_{ij} \cdot (\vec{u}_i + \vec{u}_j)) \vec{z}_{ij} \right\} \quad (20)$$

where Q is the total energy that flows through the non-thermostated walls, A_s is the wall surface area in contact with water, Δt is the elapsed time, V is the volume of the simulation domain, e_i is the internal energy of the atom, $u_{i,z}$ is the velocity of the i -th atom in the z direction, u_i and u_j are the velocities of atoms i and j , respectively, \vec{f}_{ij} is the pairwise force between different atoms, and \vec{z}_{ij} is the position vector between atoms i and j .

Conventionally, the quantification of convective heat transfer is characterized using the non-dimensional Nusselt number, Nu_D , which is the ratio of convection to conduction normal to the interface. By combining Equations (18)–(20), the Nu_D can be calculated as

$$Nu_D = \frac{hD_h}{h_f} = \frac{2Hq_s''}{\lambda(T_w - T_m(x))} \quad (21)$$

where λ represents the thermal conductivity of the fluid. In the absence of advection effects, q_s'' is equivalent to the conduction heat flux through water in the z direction at the channel surface, given by $q_s'' = -\lambda \left(\frac{\partial T}{\partial z} \right)_{z=0}$. The coefficients h and Nu_D are also determined using the conduction heat flux based on the temperature gradient at the wall:

$$h = \frac{\lambda}{T_w - T_m(x)} \left. \frac{\partial T}{\partial z} \right|_{z=0} \quad (22)$$

and

$$Nu_D = \frac{hD_h}{h_f} = \frac{2H}{T_w - T_m(x)} \left. \frac{\partial T}{\partial z} \right|_{z=0} \quad (23)$$

In flow simulations, periodic boundary conditions are usually applied, often paired with a constant flow-driving force applied to each of the fluid atoms or molecules in the flow direction. This setup enables the liquid to exit through one side of the periodic box (outlet) and re-enter across the periodic boundary (inlet). In earlier MD studies on Poiseuille flow [41,100,212], an external force was applied uniformly to each liquid molecule similar to that of a gravity-driven flow. This approach led to a significant injection of energy into the system, therefore temperature control was enforced on both the wall and the fluid molecules, which potentially generates less realistic results. To better simulate a pressure-driven flow and attain more accurate outcomes, the external force can be exclusively applied at the inlet region of the channel. This adjustment ensures a more physically significant simulation. However, because of the supplementary energy introduced by the body force, and the existence of a temperature gradient within the channel, the energy conservation between the inlet and outlet is not maintained. This leads to distortions in the convective heat transfer process. In some cases, this issue is improved by a strategy called thermal pump method [42,221]. This method partitions the fluid domain into several distinct regions, specifically: a forcing zone, a temperature reset zone, and a data collection zone; one example is illustrated in Figure 10.

Based on this temperature control strategy, some works have discussed the Poiseuille flow convective heat transfer under periodic boundary conditions. Motlagh and Kaltech [226,227] conducted an extensive study on convective heat transfer in nanochannels, focusing on two main aspects: the effect of the wall roughness and the effect of nanoparticles; a similar work was also conducted by Chakraborty et al. [228]. These findings were validated by comparing the Nusselt number with the results presented by Ge et al. [221]. In this work, special attention was given to thermal slip and its impact on the convective heat transfer of Poiseuille flow; in addition, the influence of wettability on Nu was also discussed. Dinh et al. [103] studied the viscous heating of water flows in copper nanochannels, by simulating two scenarios: Couette flows and Poiseuille flows. The scale effects on the distribution of fluid density, streaming velocity, fluid viscosity and temperature across the channel were discussed. Results show that surface forces cause a large difference between the simulation results and the continuum theory. Toghraie et al. [229] also conducted simulations on heat transfer in Couette and Poiseuille water flows with copper walls, considering both smooth and rough nanochannels. They noted that an increase in the channel height led to a reduction of the surface effect on the liquid, resulting into a decrease of the nanofluid flow rate.

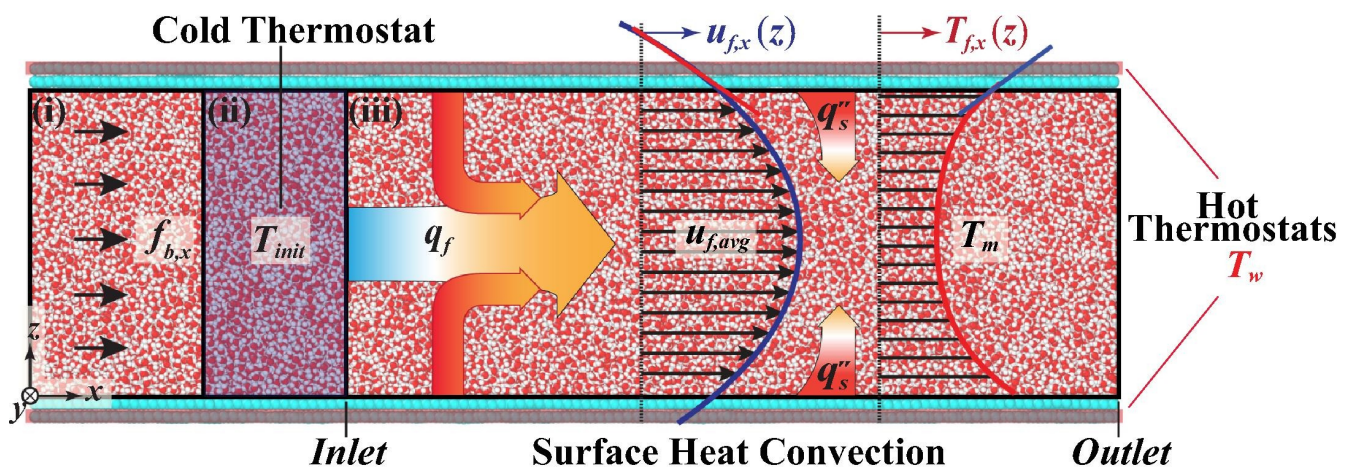


Figure 10. Schematic illustration of the thermal pump method. The simulation domain is divided into three regions: (i) the forcing region, to set the fluid velocity; (ii) the temperature rescaling region, to set the inlet temperature; and (iii) the data collection region. Reprinted from [225] with permission.

3.3. Two Phase Flow in Nanochannels

In practical applications, especially in extremely small systems such as nanoscale semiconductor devices, nano- and atomic-scale fluid flows, along with nanoscale ultra-fast evaporation, single-phase flow heat exchangers are not as common as those involving multi-phase flow. Understanding convective heat transfer in single-phase flow provides a foundation, but the phenomenon and mechanisms become more complicated when it comes to multi-phase flow in nanochannels. This complexity is particularly significant in processes such as heating and cooling, which correspond to boiling and condensation. As described previously, boiling involves the rapid phase transition from liquid to vapour, accompanied by the formation of vapour bubbles. MD simulations enable a detailed examination of bubble nucleation, growth, and departure during boiling. When this occurs in a nanochannel, due to the confinement of fluid flow, the behaviour differs significantly from larger-scale flows. Similarly, condensation is the opposite of boiling, involving the phase transition from vapour back to liquid. Discrepancies in flow patterns, density, and temperature distributions arise between the nanoscale and the macroscale. These phenomena, characterized by features like large slip lengths and ballistic gas transport, present interesting prospects for nanoscale two-phase thermal management devices.

Dong et al. [27] conducted molecular dynamics simulations of R141b boiling flow in a nanochannel. They analysed the temperature distribution, density, and surface tension profiles in a cuboid cell with a temperature gradient applied to both walls. Their findings indicated that the characteristics of the liquid-vapour interface were strongly influenced by the saturation temperature and the degree of superheat. Ji and Yan [32] studied the behaviour of a liquid-vapour-solid system near the triple-point of flow boiling in a microchannel heat sink. They found that key parameters influencing the system include the number of fluid atoms, the temperature of the solid wall, and the size of the simulation. Cao et al. [217] conducted simulations of the liquid-vapour co-existence in nanostructured channels. Two different wettabilities have been considered, and they found that the wetting models of fluid over the nanostructured surface are quite different for the hydrophobic and hydrophilic liquid-solid interactions. In the case of a hydrophobic liquid-solid interaction, the liquid droplet partially spread over the peaks of the surface nanostructures. The gaps within the nanostructure were not entirely filled, resulting into a lower density of the liquid near the surfaces. On the other hand, for the hydrophilic liquid-solid interaction, the fluid is able to fully wet the surface of nanostructures, and wetting becomes homogeneous. Due to the confined space in microchannel heat sinks, bubbles and slugs display unique shapes compared to those in larger-scale channels. These bubbles and slugs exhibit an elongated shape in the flow direction, and occupy most of the channel cross-section. In other words, the bubbles and slugs in boiling inside microchannels resemble annular flow, except for the presence of a liquid bridge between consecutive slugs. Thus, annular flow can be viewed as the representative flow pattern in microchannel flow boiling. In microchannel heat sinks with annular flow, the entire flow field can be divided into two zones: continuous vapour along the centre of the channel, and an annular liquid film along the channel wall.

Alongside the continuous liquid film, dispersed liquid droplets may be entrained in the continuous vapour phase, as observed by Jiang et al. [230] and Qu and Mudawar [231]. In annular flow, there is a simultaneous exchange of both heat and mass at the liquid-vapour interface. There is a mass exchange across the interface as liquid vaporizes and vapour condenses, carrying thermal energy. Additionally, dispersed liquid droplets undergo evaporation and deposition, leading to further heat and mass transfer. This means that, on a microscopic scale, the apparently balanced state of the annular flow interface is actually a dynamic non-equilibrium process.

Semiromi and Azimian [26] predicted the superheated flow boiling heat transfer characteristics in a nanochannel by MD simulations obtaining a similar conclusion as Dong et al. [27]. Their results indicate that saturation condition and the degree of superheat have a great influence on the surface tension in small channels. Surface tension, as described by Maruyama [232], at the liquid-vapour interface can be expressed as:

$$\gamma_{LV} = \int_0^{L_z} (P_N(z) - P_T(z)) dz \quad (24)$$

where $P_N(z)$ and $P_T(z)$ are the local normal and tangential pressure components, respectively, determined as follows [26]:

$$P_N(z) = n(z)k_B T - \frac{1}{2A} \left\{ \sum_{i \neq j} \frac{z_{ij} \phi'(r_{ij})}{r_{ij}} \theta \left(\frac{z - z_i}{z_{ij}} \right) \theta \left(\frac{z_j - z}{z_{ij}} \right) \right\} \quad (25)$$

$$P_T(z) = n(z)k_B T - \frac{1}{4A} \left\{ \sum_{i \neq j} \frac{(x_{ij}^2 + y_{ij}^2) \phi'(r_{ij})}{r_{ij} z_{ij}} \theta \left(\frac{z - z_i}{z_{ij}} \right) \theta \left(\frac{z_j - z}{z_{ij}} \right) \right\} \quad (26)$$

where $n(z)$ is the value of density at the height z , the $i \neq j$ notation indicates a summation over all distinct pairs i and j without counting any pair twice (i.e., as ij and ji). k_B is the Boltzmann constant, and $\{\}$ denotes an ensemble average taken over the duration of the simulation during which the system can be considered at thermal equilibrium.

Figure 11 illustrates the local surface tension profile perpendicular to the interface at a saturation temperature of 84 K, considering various external forces. Each surface tension curve exhibits two peaks due to the presence of two interfacial zones within the simulation cell. These curves exhibit significant fluctuations as they cross the liquid-vapour interface zone, peaking at the centre of the interface zone and then spreading out in the vapour regions. Notably, the external force at the nanochannel inlet shows no significant influence on the local surface tension profiles, suggesting that the shape of these profiles remains consistent. This implies that the local surface tension remains independent of the inlet driving force.

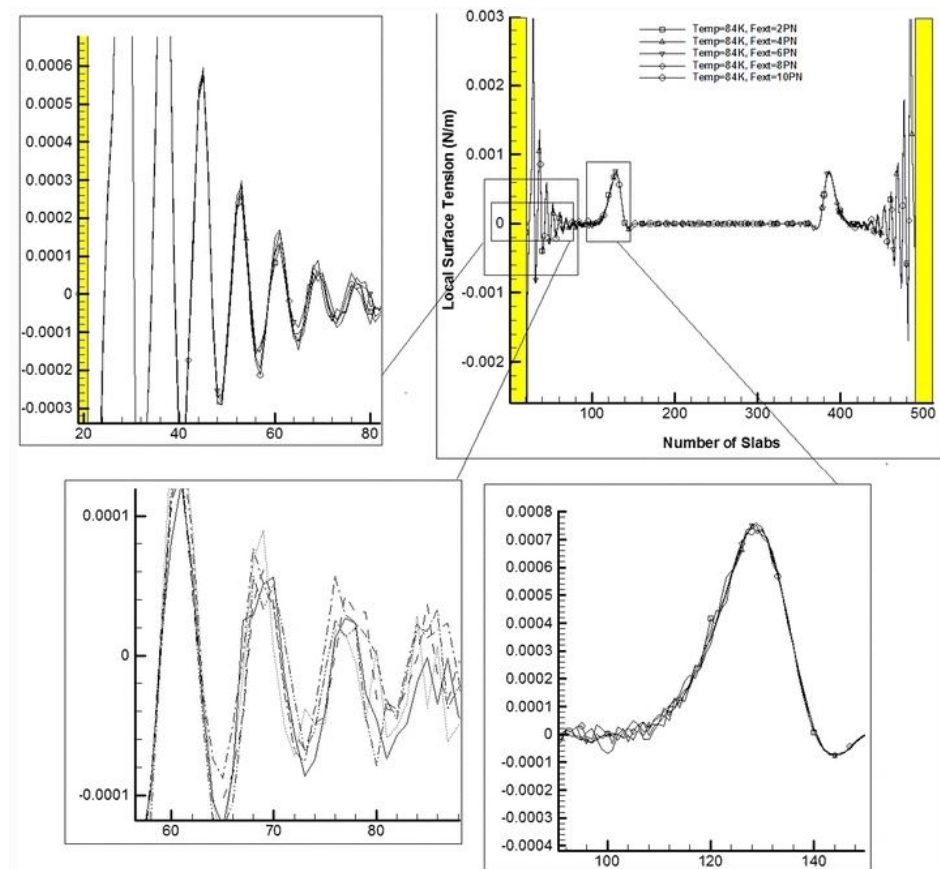


Figure 11. Local surface tension profile in the direction normal to the interface at a saturation temperature of 84 K, for different external driving forces. Reprinted from [26] with permission.

Additionally, the density profiles for any location at the liquid-solid interface remain consistent regardless of variations in external driving forces, and of the degree of superheat at the bottom wall. This suggests that the interfacial density distribution is stable and not significantly influenced by these factors. This observation could have implications for understanding and predicting the behaviour of the system under different conditions. The interface between the liquid film and the vapour core is fairly smooth, leading to a stabilization of the mean velocities of the vapor core and liquid film along the stream-wise direction (x-direction), resulting into a flow pattern characteristic of annular flow. This finding is consistent with similar observations made in other studies, such as the work conducted by Qu and Mudawar [231,233]. These results highlight the significant role that surface tension plays in determining the flow behaviour in these confined geometries.

Seyf and Zhang [73] employed Molecular Dynamics simulations to investigate the boiling behaviour of argon films on surfaces, comparing cases with and without spherical nanostructures. Their findings demonstrated that, in the presence of surface nanostructures, the liquid argon rapidly vaporized from the surface and gave rise to multiple small

liquid clusters when the argon layers closest to the solid surface experienced overheating. Fu et al. [38] conducted a study on the influence of nanostructures on the rapid boiling of water, which was rapidly heated by a hot copper plate. Zarringhalam et al. [234] studied the boiling flow behaviour of argon fluid inside microchannels with different wall temperatures. They controlled the surface temperature at 84 K, 96 K, 108 K, 114 K, 133 K, and compared the results obtained with smooth walls with those obtained in presence of roughness elements on the microchannel wall. It was found the presence of roughness elements with conical shape causes a reduction in the flow velocity as large as 0.5–1.5%.

In summary, extensive research has been conducted on fluid flow in nanochannels, encompassing discussions and analyses of both hydrodynamic and heat transfer characteristics. The primary distinction in nanochannel flow, compared to macro-scale flow, lies in the presence of hydrodynamic and thermal slip. Additionally, due to fluid confinement, unique phenomena are observed. However, research in this area still faces some challenges. Current studies often analyse very small simulation cells, which may not fully replicate realistic environments. Limited computational resources make it challenging to simulate channels of sufficient length, especially for two-phase flows, where fully developed flows and complete phase change processes can be challenging to observe due to relatively high stream velocities and short lengths. Furthermore, while some results have been obtained, their experimental validation remains a complex task in the current stage of research.

4. Challenges and Scope for Future Studies

While substantial research has been conducted in heat transfer and fluid dynamics, the application of MD simulations in these areas continues to face numerous challenges.

Firstly, MD simulations suffer from limitations in the system size and time scale. While they are suitable to model small-scale systems over short durations, they encounter difficulties when applied to larger, more complex scenarios or processes occurring over extended periods. In addition, MD simulations treat molecules from a purely mechanistic point of view, therefore they cannot describe quantum effects, which may be significant especially in environments characterized by low temperatures or high reactivity, and electromagnetic fields, which are relevant to biological systems.

Furthermore, the accuracy of force fields stands as another critical challenge. Finding the correct balance between computational efficiency and accuracy in representing intermolecular interactions remains a complex undertaking. Moreover, a smooth integration of MD simulations with other computational techniques to address multi-scale phenomena is a difficult task.

Achieving thermal equilibrium and ensuring adequate sampling of the phase space are critical for producing reliable results. This becomes especially difficult in systems with complex interfaces. A correct description of the interactions at boundaries and interfaces requires specialized techniques and careful consideration of the system geometry.

In addition, management of computational resources, including parallelization, represents a substantial challenge. Executing large-scale MD simulations requires significant computational power. Ensuring efficient parallelization and optimization of codes for high-performance computing architectures is crucial to overcome limitations in computational resources. Additionally, integrating simulation results with experimental observations can be complex due to differences in scale and precision, as well as uncertainties in the experimental measurements.

Specific items that will likely attract the main research efforts in the future are:

- Bridging the gap between molecular-level insights and macroscopic behavior through the integration of MD simulations with other computational techniques;
- The design of nanoscale heat exchangers, lab-on-a-chip devices, and the development of advanced thermal materials;
- Meeting the demand for increased computational resources to simulate larger and more complex systems;

- Improving intermolecular potentials for specific substances and conditions, especially in the area of life sciences, will enhance the accuracy of simulations.
- Developing suitable potentials to model the interactions between fluids and walls with complex molecular structure (e.g., polymer materials).

In conclusion, while MD simulations have significantly improved our understanding of thermofluid systems at the molecular level, various challenges have not been fully resolved to date. Addressing these challenges through innovative methodologies and the technology advances in computational resources will continue to expand the applicability and accuracy of MD simulations in thermofluid sciences, paving the way for groundbreaking discoveries in this field.

Author Contributions: Writing—original draft preparation, Y.R.; writing—review and editing, V.B. All authors have read and agreed to the published version of the manuscript.

Funding: This work received no external funding.

Data Availability Statement: Not applicable.

Acknowledgments: Yunmin Ran gratefully acknowledges a China Scholarship Council studentship.

Conflicts of Interest: The author declares no conflict of interest.

References

1. Abgrall, P.; Nguyen, N.T. Nanofluidic devices and their applications. *Anal. Chem.* **2008**, *80*, 2326–2341. [\[CrossRef\]](#) [\[PubMed\]](#)
2. Duan, C.; Wang, W.; Xie, Q. Fabrication of nanofluidic devices. *Biomicrofluidics* **2013**, *7*, 26501. [\[CrossRef\]](#) [\[PubMed\]](#)
3. Gad-el Hak, M. *MEMS: Introduction and Fundamentals*; CRC Press: Boca Raton, FL, USA, 2005.
4. Goh, P.; Ismail, A.; Ng, B. Carbon nanotubes for desalination: Performance evaluation and current hurdles. *Desalination* **2013**, *308*, 2–14. [\[CrossRef\]](#)
5. Bhirde, A.A.; Patel, V.; Gavard, J.; Zhang, G.; Sousa, A.A.; Masedunskas, A.; Leapman, R.D.; Weigert, R.; Gutkind, J.S.; Rusling, J.F. Targeted killing of cancer cells in vivo and in vitro with EGF-directed carbon nanotube-based drug delivery. *ACS Nano* **2009**, *3*, 307–316. [\[CrossRef\]](#) [\[PubMed\]](#)
6. Wang, Z.; Lee, I.; Jeon, T.J.; Kim, S.M. Micro-/nanofluidic device for tunable generation of a concentration gradient: Application to *Caenorhabditis elegans* chemotaxis. *Anal. Bioanal. Chem.* **2014**, *406*, 2679–2686. [\[CrossRef\]](#) [\[PubMed\]](#)
7. Dror, R.O.; Dirks, R.M.; Grossman, J.; Xu, H.; Shaw, D.E. Biomolecular simulation: A computational microscope for molecular biology. *Annu. Rev. Biophys.* **2012**, *41*, 429–452. [\[CrossRef\]](#)
8. Allen, M.P.; Tildesley, D.J. *Computer Simulation of Liquids*; Oxford University Press: Oxford, UK, 2017.
9. Leach, A.R. *Molecular Modelling: Principles and Applications*; Pearson Education: London, UK, 2001.
10. Rapaport, D.C. *The Art of Molecular Dynamics Simulation*; Cambridge University Press: Cambridge, UK, 2004.
11. Nosé, S. A unified formulation of the constant temperature molecular dynamics methods. *J. Chem. Phys.* **1984**, *81*, 511–519. [\[CrossRef\]](#)
12. Parrinello, M.; Rahman, A. Polymorphic transitions in single crystals: A new molecular dynamics method. *J. Appl. Phys.* **1981**, *52*, 7182–7190. [\[CrossRef\]](#)
13. Hockney, R.W.; Eastwood, J.W. *Computer Simulation Using Particles*; CRC Press: Boca Raton, FL, USA, 2021.
14. Alder, B.J.; Wainwright, T.E. Phase transition for a hard sphere system. *J. Chem. Phys.* **1957**, *27*, 1208–1209. [\[CrossRef\]](#)
15. Gibson, J.; Golland, A.N.; Milgram, M.; Vineyard, G. Dynamics of radiation damage. *Phys. Rev.* **1960**, *120*, 1229. [\[CrossRef\]](#)
16. Rahman, A. Correlations in the motion of atoms in liquid argon. *Phys. Rev.* **1964**, *136*, A405. [\[CrossRef\]](#)
17. Steinfeld, J.I.; Francisco, J.S.; Hase, W.L. *Chemical Kinetics and Dynamics*; Prentice Hall: Upper Saddle River, NJ, USA, 1999.
18. Andersen M.; Panosetti, C.; Reuter, R. A Practical Guide to Surface Kinetic Monte Carlo Simulations. *Front. Chem.* **2019**, *7*, 202. [\[CrossRef\]](#)
19. Bagayoko, D. Understanding density functional theory (DFT) and completing it in practice. *AIP Adv.* **2014**, *4*, 127104. [\[CrossRef\]](#)
20. Casida, M.E.; Huix-Rotllant, M. Many-Body Perturbation Theory (MBPT) and Time-Dependent Density-Functional Theory (TD-DFT): MBPT Insights About What Is Missing In, and Corrections To, the TD-DFT Adiabatic Approximation. In *Density-Functional Methods for Excited States*; Springer International Publishing: Cham, Switzerland, 2016; pp. 1–60. [\[CrossRef\]](#)
21. Allen, M.P. Introduction to molecular dynamics simulation. *Comput. Soft Matter Synth. Polym. Proteins* **2004**, *23*, 1–28.
22. Haile, J.M. *Molecular Dynamics Simulation: Elementary Methods*; John Wiley & Sons, Inc.: Hoboken, NJ, USA, 1992.
23. Maruyama, S. Molecular dynamics method for microscale heat transfer. In *Advances in Numerical Heat Transfer, Volume 2*; CRC Press: Boca Raton, FL, USA, 2018; pp. 189–226.
24. Frenkel, D.; Smit, B. *Understanding Molecular Simulation: From Algorithms To Applications*; Elsevier: Amsterdam, The Netherlands, 2023.

25. Kalweit, M.; Drikakis, D. Coupling strategies for hybrid molecular—Continuum simulation methods. *Proc. Inst. Mech. Eng. Part J. Mech. Eng. Sci.* **2008**, *222*, 797–806. [\[CrossRef\]](#)
26. Semiromi, D.T.; Azimian, A. Molecular dynamics simulation of annular flow boiling with the modified Lennard-Jones potential function. *Heat Mass Transf.* **2012**, *48*, 141–152. [\[CrossRef\]](#)
27. Dong, T.; Yang, Z.; Wu, H. Molecular simulations of R141b boiling flow in micro/nano channel: Interfacial phenomena. *Energy Convers. Manag.* **2006**, *47*, 2178–2191. [\[CrossRef\]](#)
28. Long, L.N.; Micci, M.M.; Wong, B.C. Molecular dynamics simulations of droplet evaporation. *Comput. Phys. Commun.* **1996**, *96*, 167–172. [\[CrossRef\]](#)
29. Lukes, J.R.; Li, D.; Liang, X.G.; Tien, C.L. Molecular dynamics study of solid thin-film thermal conductivity. *J. Heat Transf.* **2000**, *122*, 536–543. [\[CrossRef\]](#)
30. Matsumoto, M.; Wakabayashi, H.; Makino, T. Thermal resistance of crystal interface: Molecular dynamics simulation. *Heat-Transf. Asian Res. Spons. Soc. Chem. Eng. Jpn. Heat Transf. Div. ASME* **2005**, *34*, 135–146. [\[CrossRef\]](#)
31. Maroo, S.C.; Chung, J. A novel fluid–wall heat transfer model for molecular dynamics simulations. *J. Nanoparticle Res.* **2010**, *12*, 1913–1924. [\[CrossRef\]](#)
32. Ji, C.; Yan, Y. A molecular dynamics simulation of liquid–vapour–solid system near triple-phase contact line of flow boiling in a microchannel. *Appl. Therm. Eng.* **2008**, *28*, 195–202. [\[CrossRef\]](#)
33. Consolini, L.; Aggarwal, S.K.; Murad, S. A molecular dynamics simulation of droplet evaporation. *Int. J. Heat Mass Transf.* **2003**, *46*, 3179–3188. [\[CrossRef\]](#)
34. Røsjorde, A.; Fossmo, D.; Bedeaux, D.; Kjelstrup, S.; Hafskjold, B. Nonequilibrium molecular dynamics simulations of steady-state heat and mass transport in condensation: I. Local equilibrium. *J. Colloid Interface Sci.* **2000**, *232*, 178–185. [\[CrossRef\]](#)
35. Røsjorde, A.; Kjelstrup, S.; Bedeaux, D.; Hafskjold, B. Nonequilibrium molecular dynamics simulations of steady-state heat and mass transport in condensation. II. Transfer coefficients. *J. Colloid Interface Sci.* **2001**, *240*, 355–364. [\[CrossRef\]](#)
36. Maroo, S.C.; Chung, J. Molecular dynamic simulation of platinum heater and associated nano-scale liquid argon film evaporation and colloidal adsorption characteristics. *J. Colloid Interface Sci.* **2008**, *328*, 134–146. [\[CrossRef\]](#)
37. Nagayama, G.; Tsuruta, T.; Cheng, P. Molecular dynamics simulation on bubble formation in a nanochannel. *Int. J. Heat Mass Transf.* **2006**, *49*, 4437–4443. [\[CrossRef\]](#)
38. Fu, T.; Mao, Y.; Tang, Y.; Zhang, Y.; Yuan, W. Effect of nanostructure on rapid boiling of water on a hot copper plate: A molecular dynamics study. *Heat Mass Transf.* **2016**, *52*, 1469–1478. [\[CrossRef\]](#)
39. Xue, L.; Keblinski, P.; Phillpot, S.; Choi, S.S.; Eastman, J. Two regimes of thermal resistance at a liquid–solid interface. *J. Chem. Phys.* **2003**, *118*, 337–339. [\[CrossRef\]](#)
40. Wang, Y.H.; Wang, S.Y.; Lu, G.; Wang, X.D. Explosive boiling of nano-liquid argon films on high temperature platinum walls: Effects of surface wettability and film thickness. *Int. J. Therm. Sci.* **2018**, *132*, 610–617. [\[CrossRef\]](#)
41. Barrat, J.L.; Bocquet, L. Influence of wetting properties on hydrodynamic boundary conditions at a fluid/solid interface. *Faraday Discuss.* **1999**, *112*, 119–128. [\[CrossRef\]](#)
42. Markvoort, A.J.; Hilbers, P.; Nede, S. Molecular dynamics study of the influence of wall-gas interactions on heat flow in nanochannels. *Phys. Rev. E* **2005**, *71*, 066702. [\[CrossRef\]](#) [\[PubMed\]](#)
43. Yang, S.C. Effects of surface roughness and interface wettability on nanoscale flow in a nanochannel. *Microfluid. Nanofluidics* **2006**, *2*, 501–511. [\[CrossRef\]](#)
44. Inaoka, H.; Ito, N. Numerical simulation of pool boiling of a Lennard-Jones liquid. *Phys. A Stat. Mech. Its Appl.* **2013**, *392*, 3863–3868. [\[CrossRef\]](#)
45. Wu. A molecular dynamics simulation of bubble nucleation in homogeneous liquid under heating with constant mean negative pressure. *Microscale Thermophys. Eng.* **2003**, *7*, 137–151. [\[CrossRef\]](#)
46. Kinjo, T.; Matsumoto, M. Cavitation processes and negative pressure. *Fluid Phase Equilibria* **1998**, *144*, 343–350. [\[CrossRef\]](#)
47. Yamamoto, T.; Matsumoto, M. Initial stage of nucleate boiling: Molecular dynamics investigation. *J. Therm. Sci. Technol.* **2012**, *7*, 334–349. [\[CrossRef\]](#)
48. Hens, A.; Agarwal, R.; Biswas, G. Nanoscale study of boiling and evaporation in a liquid Ar film on a Pt heater using molecular dynamics simulation. *Int. J. Heat Mass Transf.* **2014**, *71*, 303–312. [\[CrossRef\]](#)
49. Sumardiono, S.; Fischer, J. Molecular simulations of droplet evaporation processes: Adiabatic pressure jump evaporation. *Int. J. Heat Mass Transf.* **2006**, *49*, 1148–1161. [\[CrossRef\]](#)
50. Niu, D.; Tang, G. The effect of surface wettability on water vapor condensation in nanoscale. *Sci. Rep.* **2016**, *6*, 19192. [\[CrossRef\]](#)
51. Sheng, Q.; Sun, J.; Wang, Q.; Wang, W.; Wang, H.S. On the onset of surface condensation: Formation and transition mechanisms of condensation mode. *Sci. Rep.* **2016**, *6*, 30764. [\[CrossRef\]](#) [\[PubMed\]](#)
52. Gu, K.; Watkins, C.B.; Koplik, J. Molecular dynamics simulation of the equilibrium liquid–vapor interphase with solidification. *Fluid Phase Equilibria* **2010**, *297*, 77–89. [\[CrossRef\]](#)
53. Fujinaga, T.; Shibuta, Y. Molecular dynamics simulation of athermal heterogeneous nucleation of solidification. *Comput. Mater. Sci.* **2019**, *164*, 74–81. [\[CrossRef\]](#)
54. Cui, S.; Cummings, P.; Cochran, H. Molecular simulation of the transition from liquidlike to solidlike behavior in complex fluids confined to nanoscale gaps. *J. Chem. Phys.* **2001**, *114*, 7189–7195. [\[CrossRef\]](#)

55. Geiser, J. Coupled Navier–Stokes molecular dynamics simulation: Theory and applications based on iterative operator-splitting methods. *Comput. Fluids* **2013**, *77*, 97–111. [\[CrossRef\]](#)
56. Asproulis, N.; Drikakis, D. An artificial neural network-based multiscale method for hybrid atomistic-continuum simulations. *Microfluid. Nanofluid.* **2013**, *15*, 559–574. [\[CrossRef\]](#)
57. Werder, T.; Walther, J.H.; Koumoutsakos, P. Hybrid atomistic-continuum method for the simulation of dense fluid flows. *J. Comput. Phys.* **2005**, *205*, 373–390. [\[CrossRef\]](#)
58. Stephenson, D.; Lockerby, D.A.; Borg, M.K.; Reese, J.M. Multiscale simulation of nanofluidic networks of arbitrary complexity. *Microfluid. Nanofluid.* **2015**, *18*, 841–858. [\[CrossRef\]](#)
59. Borg, M.K.; Lockerby, D.A.; Reese, J.M. A hybrid molecular-continuum method for unsteady compressible multiscale flows. *J. Fluid Mech.* **2015**, *768*, 388–414. [\[CrossRef\]](#)
60. Holland, D.M.; Lockerby, D.A.; Borg, M.K.; Nicholls, W.D.; Reese, J.M. Molecular dynamics pre-simulations for nanoscale computational fluid dynamics. *Microfluid. Nanofluid.* **2015**, *18*, 461–474. [\[CrossRef\]](#)
61. Bertola, V.; Cafaro, E. On the speed of heat. *Phys. Lett. Sect. Gen. At. Solid State Phys.* **2007**, *372*, 1–4. [\[CrossRef\]](#)
62. Lu, W.Q.; Fan, Q.M. Study for the particle's scale effect on some thermophysical properties of nanofluids by a simplified molecular dynamics method. *Eng. Anal. Bound. Elem.* **2008**, *32*, 282–289. [\[CrossRef\]](#)
63. Tuckerman, M.E. *Statistical Mechanics: Theory and Molecular Simulation*; Oxford University Press: Oxford, UK, 2023.
64. Müller-Plathe, F. A simple nonequilibrium molecular dynamics method for calculating the thermal conductivity. *J. Chem. Phys.* **1997**, *106*, 6082–6085. [\[CrossRef\]](#)
65. Schneider, T.; Stoll, E. Molecular-dynamics study of a three-dimensional one-component model for distortive phase transitions. *Phys. Rev. B* **1978**, *17*, 1302. [\[CrossRef\]](#)
66. Schelling, P.; Phillpot, S.; Keblinski, P. Phonon wave-packet dynamics at semiconductor interfaces by molecular-dynamics simulation. *Appl. Phys. Lett.* **2002**, *80*, 2484–2486. [\[CrossRef\]](#)
67. Plimpton, S. Fast parallel algorithms for short-range molecular dynamics. *J. Comput. Phys.* **1995**, *117*, 1–19. [\[CrossRef\]](#)
68. Yezdimer, E.M.; Chialvo, A.A.; Cummings, P.T. Examination of chain length effects on the solubility of alkanes in near-critical and supercritical aqueous solutions. *J. Phys. Chem. B* **2001**, *105*, 841–847. [\[CrossRef\]](#)
69. Delhomelle, J.; Millié, P. Inadequacy of the Lorentz-Berthelot combining rules for accurate predictions of equilibrium properties by molecular simulation. *Mol. Phys.* **2001**, *99*, 619–625. [\[CrossRef\]](#)
70. Wang, C.; Chen, J.; Shiomi, J.; Maruyama, S. A study on the thermal resistance over solid-liquid-vapor interfaces in a finite-space by a molecular dynamics method. *Int. J. Therm. Sci.* **2007**, *46*, 1203–1210. [\[CrossRef\]](#)
71. Ohara, T. Contribution of intermolecular energy transfer to heat conduction in a simple liquid. *J. Chem. Phys.* **1999**, *111*, 9667–9672. [\[CrossRef\]](#)
72. Chen, Y.; Zou, Y.; Sun, D.; Wang, Y.; Yu, B. Molecular dynamics simulation of bubble nucleation on nanostructure surface. *Int. J. Heat Mass Transf.* **2018**, *118*, 1143–1151. [\[CrossRef\]](#)
73. Reza Seyf, H.; Zhang, Y. Molecular dynamics simulation of normal and explosive boiling on nanostructured surface. *J. Heat Transf.* **2013**, *135*, 121503. [\[CrossRef\]](#)
74. Sun, C.; Lu, W.Q.; Liu, J.; Bai, B. Molecular dynamics simulation of nanofluid's effective thermal conductivity in high-shear-rate Couette flow. *Int. J. Heat Mass Transf.* **2011**, *54*, 2560–2567. [\[CrossRef\]](#)
75. Toghraie, D.; Mokhtari, M.; Afrand, M. Molecular dynamic simulation of copper and platinum nanoparticles Poiseuille flow in a nanochannels. *Phys. E -Low-Dimens. Syst. Nanostruct.* **2016**, *84*, 152–161. [\[CrossRef\]](#)
76. Jónsson, E.Ö.; Rasti, S.; Galynska, M.; Meyer, J.; Jónsson, H. Transferable Potential Function for Flexible H₂O Molecules Based on the Single-Center Multipole Expansion. *J. Chem. Theory Comput.* **2022**, *18*, 7528–7543. [\[CrossRef\]](#)
77. Sofos, F.; Karakasidis, T.; Liakopoulos, A. Transport properties of liquid argon in krypton nanochannels: Anisotropy and non-homogeneity introduced by the solid walls. *Int. J. Heat Mass Transf.* **2009**, *52*, 735–743. [\[CrossRef\]](#)
78. Hu, H.; Sun, Y. Effect of nanopatterns on Kapitza resistance at a water-gold interface during boiling: A molecular dynamics study. *J. Appl. Phys.* **2012**, *112*. [\[CrossRef\]](#)
79. Ghorbanian, J.; Beskok, A. Scale effects in nano-channel liquid flows. *Microfluid. Nanofluid.* **2016**, *20*, 1–11. [\[CrossRef\]](#)
80. Al-Matar, A.K.; Rockstraw, D.A. A generating equation for mixing rules and two new mixing rules for interatomic potential energy parameters. *J. Comput. Chem.* **2004**, *25*, 660–668. [\[CrossRef\]](#)
81. Thomas, J.A.; McGaughey, A.J.; Kuter-Arnebeck, O. Pressure-driven water flow through carbon nanotubes: Insights from molecular dynamics simulation. *Int. J. Therm. Sci.* **2010**, *49*, 281–289. [\[CrossRef\]](#)
82. Thomas, J.A.; McGaughey, A.J. Reassessing fast water transport through carbon nanotubes. *Nano Lett.* **2008**, *8*, 2788–2793. [\[CrossRef\]](#)
83. Alosious, S.; Kannam, S.K.; Sathian, S.P.; Todd, B. Nanoconfinement effects on the kapitza resistance at water-cnt interfaces. *Langmuir* **2021**, *37*, 2355–2361. [\[CrossRef\]](#)
84. Hafskjold, B.; Ikeshoji, T.; Ratkje, S.K. On the molecular mechanism of thermal diffusion in liquids. *Mol. Phys.* **1993**, *80*, 1389–1412. [\[CrossRef\]](#)
85. Ikeshoji, T.; Hafskjold, B. Non-equilibrium molecular dynamics calculation of heat conduction in liquid and through liquid-gas interface. *Mol. Phys.* **1994**, *81*, 251–261. [\[CrossRef\]](#)

86. Irving, J.; Kirkwood, J.G. The statistical mechanical theory of transport processes. IV. The equations of hydrodynamics. *J. Chem. Phys.* **1950**, *18*, 817–829. [\[CrossRef\]](#)
87. Tokumasu, T.; Ohara, T.; Kamijo, K. Effect of molecular elongation on the thermal conductivity of diatomic liquids. *J. Chem. Phys.* **2003**, *118*, 3677–3685. [\[CrossRef\]](#)
88. Kim, B.H.; Beskok, A.; Cagin, T. Thermal interactions in nanoscale fluid flow: Molecular dynamics simulations with solid–liquid interfaces. *Microfluid. Nanofluid.* **2008**, *5*, 551–559. [\[CrossRef\]](#)
89. Barrat, J.L.; Chiaruttini, F. Kapitza resistance at the liquid–solid interface. *Mol. Phys.* **2003**, *101*, 1605–1610. [\[CrossRef\]](#)
90. Sarode, A.; Ahmed, Z.; Basarkar, P.; Bhargav, A.; Banerjee, D. Role of carbon nanotube on the interfacial thermal resistance: A molecular dynamics approach. In Proceedings of the 2017 16th IEEE Intersociety Conference on Thermal and Thermomechanical Phenomena in Electronic Systems (ITherm), Orlando, FL, USA, 30 May–2 June 2017; pp. 352–356.
91. Lautenschlaeger, M.P.; Hasse, H. Thermal, caloric and transport properties of the Lennard–Jones truncated and shifted fluid in the adsorbed layers at dispersive solid walls. *Mol. Phys.* **2020**, *118*, e1669838. [\[CrossRef\]](#)
92. de Gennes, P.G. On fluid/wall slippage. *Langmuir* **2002**, *18*, 3413–3414. [\[CrossRef\]](#)
93. Bonaccorso, E.; Kappl, M.; Butt, H.J. Hydrodynamic force measurements: Boundary slip of water on hydrophilic surfaces and electrokinetic effects. *Phys. Rev. Lett.* **2002**, *88*, 076103. [\[CrossRef\]](#) [\[PubMed\]](#)
94. Bonaccorso, E.; Butt, H.J.; Craig, V.S. Surface roughness and hydrodynamic boundary slip of a Newtonian fluid in a completely wetting system. *Phys. Rev. Lett.* **2003**, *90*, 144501. [\[CrossRef\]](#) [\[PubMed\]](#)
95. Zhu, Y.; Granick, S. Limits of the hydrodynamic no-slip boundary condition. *Phys. Rev. Lett.* **2002**, *88*, 106102. [\[CrossRef\]](#) [\[PubMed\]](#)
96. Craig, V.S.; Neto, C.; Williams, D.R. Shear-dependent boundary slip in an aqueous Newtonian liquid. *Phys. Rev. Lett.* **2001**, *87*, 054504. [\[CrossRef\]](#) [\[PubMed\]](#)
97. Thompson, P.A.; Troian, S.M. A general boundary condition for liquid flow at solid surfaces. *Nature* **1997**, *389*, 360–362. [\[CrossRef\]](#)
98. Sendner, C.; Horinek, D.; Bocquet, L.; Netz, R.R. Interfacial water at hydrophobic and hydrophilic surfaces: Slip, viscosity, and diffusion. *Langmuir* **2009**, *25*, 10768–10781. [\[CrossRef\]](#)
99. Vinogradova, O.I.; Belyaev, A.V. Wetting, roughness and flow boundary conditions. *J. Phys. Condens. Matter* **2011**, *23*, 184104. [\[CrossRef\]](#)
100. Cieplak, M.; Koplik, J.; Banavar, J.R. Boundary conditions at a fluid–solid interface. *Phys. Rev. Lett.* **2001**, *86*, 803. [\[CrossRef\]](#)
101. Ohara, T.; Torii, D. Molecular dynamics study of thermal phenomena in an ultrathin liquid film sheared between solid surfaces: The influence of the crystal plane on energy and momentum transfer at solid–liquid interfaces. *J. Chem. Phys.* **2005**, *122*, 214717. [\[CrossRef\]](#)
102. Torii, D.; Ohara, T.; Ishida, K. Molecular-scale mechanism of thermal resistance at the solid–liquid interfaces: Influence of interaction parameters between solid and liquid molecules. *J. Heat Transf.* **2010**, *132*, 1–9. [\[CrossRef\]](#)
103. Dinh, Q.V.; Vo, T.Q.; Kim, B. Viscous heating and temperature profiles of liquid water flows in copper nanochannel. *J. Mech. Sci. Technol.* **2019**, *33*, 3257–3263. [\[CrossRef\]](#)
104. Koplik, J.; Banavar, J.R.; Willemsen, J.F. Molecular dynamics of fluid flow at solid surfaces. *Phys. Fluids A Fluid Dyn.* **1989**, *1*, 781–794. [\[CrossRef\]](#)
105. Bitsanis, I.; Somers, S.A.; Davis, H.T.; Tirrell, M. Microscopic dynamics of flow in molecularly narrow pores. *J. Chem. Phys.* **1990**, *93*, 3427–3431. [\[CrossRef\]](#)
106. Thompson, P.A.; Robbins, M.O. Simulations of contact-line motion: Slip and the dynamic contact angle. *Phys. Rev. Lett.* **1989**, *63*, 766. [\[CrossRef\]](#) [\[PubMed\]](#)
107. Thompson, P.A.; Robbins, M.O. Shear flow near solids: Epitaxial order and flow boundary conditions. *Phys. Rev. A* **1990**, *41*, 6830. [\[CrossRef\]](#) [\[PubMed\]](#)
108. Thompson, P.A.; Grest, G.S.; Robbins, M.O. Phase transitions and universal dynamics in confined films. *Phys. Rev. Lett.* **1992**, *68*, 3448. [\[CrossRef\]](#) [\[PubMed\]](#)
109. Somers, S.A.; Davis, H.T. Microscopic dynamics of fluids confined between smooth and atomically structured solid surfaces. *J. Chem. Phys.* **1992**, *96*, 5389–5407. [\[CrossRef\]](#)
110. Gupta, S.; Cochran, H.; Cummings, P. Shear behavior of squalane and tetracosane under extreme confinement. I. Model, simulation method, and interfacial slip. *J. Chem. Phys.* **1997**, *107*, 10316–10326. [\[CrossRef\]](#)
111. Gupta, S.; Cochran, H.; Cummings, P. Shear behavior of squalane and tetracosane under extreme confinement. II. Confined film structure. *J. Chem. Phys.* **1997**, *107*, 10327–10334. [\[CrossRef\]](#)
112. Gupta, S.; Cochran, H.; Cummings, P. Shear behavior of squalane and tetracosane under extreme confinement. III. Effect of confinement on viscosity. *J. Chem. Phys.* **1997**, *107*, 10335–10343. [\[CrossRef\]](#)
113. Jabbarzadeh, A.; Atkinson, J.; Tanner, R. Rheological properties of thin liquid films by molecular dynamics simulations. *J. Non-Newton. Fluid Mech.* **1997**, *69*, 169–193. [\[CrossRef\]](#)
114. Jabbarzadeh, A.; Atkinson, J.; Tanner, R. Effect of the wall roughness on slip and rheological properties of hexadecane in molecular dynamics simulation of Couette shear flow between two sinusoidal walls. *Phys. Rev. E* **2000**, *61*, 690. [\[CrossRef\]](#)
115. Khare, R.; De Pablo, J.; Yethiraj, A. Molecular simulation and continuum mechanics study of simple fluids in non-isothermal planar couette flows. *J. Chem. Phys.* **1997**, *107*, 2589–2596. [\[CrossRef\]](#)
116. Heinbuch, U.; Fischer, J. Liquid flow in pores: Slip, no-slip, or multilayer sticking. *Phys. Rev. A* **1989**, *40*, 1144. [\[CrossRef\]](#)

117. Todd, B.; Evans, D.J. The heat flux vector for highly inhomogeneous nonequilibrium fluids in very narrow pores. *J. Chem. Phys.* **1995**, *103*, 9804–9809. [\[CrossRef\]](#)
118. Ziarani, A.; Mohamad, A. A molecular dynamics study of perturbed Poiseuille flow in a nanochannel. *Microfluid. Nanofluid.* **2006**, *2*, 12–20. [\[CrossRef\]](#)
119. Gao, J.; Luedtke, W.; Landman, U. Structures, solvation forces and shear of molecular films in a rough nano-confinement. *Tribol. Lett.* **2000**, *9*, 3–13. [\[CrossRef\]](#)
120. Churaev, N.; Sobolev, V.; Somov, A. Slippage of liquids over lyophobic solid surfaces. *J. Colloid Interface Sci.* **1984**, *97*, 574–581. [\[CrossRef\]](#)
121. Zhu, Y.; Granick, S. Rate-dependent slip of Newtonian liquid at smooth surfaces. *Phys. Rev. Lett.* **2001**, *87*, 096105. [\[CrossRef\]](#)
122. Robbins, M.O.; Müser, M.H. Computer Simulations of Friction, Lubrication, and Wear. In *Modern Tribology Handbook, Two Volume Set*; CRC Press: Boca Raton, FL, USA, 2000; pp. 747–796.
123. Barrat, J.L.; Bocquet, L. Large slip effect at a nonwetting fluid-solid interface. *Phys. Rev. Lett.* **1999**, *82*, 4671. [\[CrossRef\]](#)
124. Heslot, F.; Fraysse, N.; Cazabat, A. Molecular layering in the spreading of wetting liquid drops. *Nature* **1989**, *338*, 640–642. [\[CrossRef\]](#)
125. Cheng, L.; Fenter, P.; Nagy, K.; Schlegel, M.; Sturchio, N. Molecular-scale density oscillations in water adjacent to a mica surface. *Phys. Rev. Lett.* **2001**, *87*, 156103. [\[CrossRef\]](#) [\[PubMed\]](#)
126. Heier, M.; Diewald, F.; Horsch, M.T.; Langenbach, K.; Müller, R.; Hasse, H. Molecular dynamics study of adsorption of the Lennard-Jones truncated and shifted fluid on planar walls. *J. Chem. Eng. Data* **2018**, *64*, 386–394. [\[CrossRef\]](#)
127. Heier, M.; Stephan, S.; Diewald, F.; Müller, R.; Langenbach, K.; Hasse, H. Molecular dynamics study of wetting and adsorption of binary mixtures of the Lennard-Jones truncated and shifted fluid on a planar wall. *Langmuir* **2021**, *37*, 7405–7419. [\[CrossRef\]](#) [\[PubMed\]](#)
128. Akkus, Y.; Nguyen, C.T.; Celebi, A.T.; Beskok, A. A first look at the performance of nano-grooved heat pipes. *Int. J. Heat Mass Transf.* **2019**, *132*, 280–287. [\[CrossRef\]](#)
129. Nguyen, C.T.; Barisik, M.; Kim, B. Wetting of chemically heterogeneous striped surfaces: Molecular dynamics simulations. *AIP Adv.* **2018**, *8*, 65003. [\[CrossRef\]](#)
130. Noh, Y.; Vo, T.; Kim, B. Subatomic-Level Solid/Fluid Boundary of Lennard-Jones Atoms: A Molecular Dynamics Study of Metal-Inert Fluid Interface. *Appl. Sci.* **2019**, *9*, 2439. [\[CrossRef\]](#)
131. Hubbard, A.T. *The Handbook of Surface Imaging and Visualization*; CRC Press: Boca Raton, FL, USA, 2022.
132. Cahill, D.G.; Braun, P.V.; Chen, G.; Clarke, D.R.; Fan, S.; Goodson, K.E.; Keblinski, P.; King, W.P.; Mahan, G.D.; Majumdar, A.; et al. Nanoscale thermal transport. II. 2003–2012. *Appl. Phys. Rev.* **2014**, *1*, 11305. [\[CrossRef\]](#)
133. Razavi, S.; Koplik, J.; Kretschmar, I. Molecular dynamics simulations: Insight into molecular phenomena at interfaces. *Langmuir* **2014**, *30*, 11272–11283. [\[CrossRef\]](#)
134. Bjornenhohn, E.; Hansen, M.; Hodgson, A.; Liu, L.; Limmer, D.; Michaelides, A.; Pedevilla, P.; Rossmeisl, J.; Shen, H.; Tocci, G.; et al. Water at Interfaces. *Chem. Rev.* **2016**, *116*, 7698–7726. [\[CrossRef\]](#)
135. Magda, J.; Tirrell, M.; Davis, H. Molecular dynamics of narrow, liquid-filled pores. *J. Chem. Phys.* **1985**, *83*, 1888–1901. [\[CrossRef\]](#)
136. Pozhar, L.A. Structure and dynamics of nanofluids: Theory and simulations to calculate viscosity. *Phys. Rev. E* **2000**, *61*, 1432. [\[CrossRef\]](#) [\[PubMed\]](#)
137. Bock, H.; Gubbins, K.E.; Schoen, M. Anisotropic self-diffusion in nanofluidic structures. *J. Phys. Chem. C* **2007**, *111*, 15493–15504. [\[CrossRef\]](#)
138. Horn, R.G.; Israelachvili, J.N. Direct measurement of structural forces between two surfaces in a nonpolar liquid. *J. Chem. Phys.* **1981**, *75*, 1400–1411. [\[CrossRef\]](#)
139. Schmitt, S.; Vo, T.; Lautenschlaeger, M.P.; Stephan, S.; Hasse, H. Molecular dynamics simulation study of heat transfer across solid–fluid interfaces in a simple model system. *Mol. Phys.* **2022**, *120*, e2057364. [\[CrossRef\]](#)
140. Akkus, Y.; Beskok, A. Molecular diffusion replaces capillary pumping in phase-change-driven nanopumps. *Microfluid. Nanofluid.* **2019**, *23*, 14. [\[CrossRef\]](#)
141. Hasan, M.R.; Vo, T.Q.; Kim, B. Manipulating thermal resistance at the solid–fluid interface through monolayer deposition. *RSC Adv.* **2019**, *9*, 4948–4956. [\[CrossRef\]](#)
142. Maruyama, S.; Kimura, T. A study on thermal resistance over a solid-liquid interface by the molecular dynamics method. *Therm. Sci. Eng* **1999**, *7*, 63–68.
143. Kim, B.H.; Beskok, A.; Cagin, T. Molecular dynamics simulations of thermal resistance at the liquid-solid interface. *J. Chem. Phys.* **2008**, *129*, 174701. [\[CrossRef\]](#) [\[PubMed\]](#)
144. Barisik, M.; Beskok, A. Temperature dependence of thermal resistance at the water/silicon interface. *Int. J. Therm. Sci.* **2014**, *77*, 47–54. [\[CrossRef\]](#)
145. Song, G.; Min, C. Temperature dependence of thermal resistance at a solid/liquid interface. *Mol. Phys.* **2013**, *111*, 903–908. [\[CrossRef\]](#)
146. Pham, A.T.; Barisik, M.; Kim, B. Interfacial thermal resistance between the graphene-coated copper and liquid water. *Int. J. Heat Mass Transf.* **2016**, *97*, 422–431. [\[CrossRef\]](#)
147. Murad, S.; Puri, I.K. Molecular simulation of thermal transport across hydrophilic interfaces. *Chem. Phys. Lett.* **2008**, *467*, 110–113. [\[CrossRef\]](#)

148. Jabbari, F.; Rajabpour, A.; Saedodin, S.; Wongwises, S. Effect of water/carbon interaction strength on interfacial thermal resistance and the surrounding molecular nanolayer of CNT and graphene flake. *J. Mol. Liq.* **2019**, *282*, 197–204. [\[CrossRef\]](#)
149. Alosious, S.; Kannam, S.K.; Sathian, S.P.; Todd, B. Kapitza resistance at water–graphene interfaces. *J. Chem. Phys.* **2020**, *152*, 224703. [\[CrossRef\]](#)
150. Alexeev, D.; Chen, J.; Walther, J.H.; Giapis, K.P.; Angelikopoulos, P.; Koumoutsakos, P. Kapitza resistance between few-layer graphene and water: Liquid layering effects. *Nano Lett.* **2015**, *15*, 5744–5749. [\[CrossRef\]](#)
151. Liang, Z.; Sasikumar, K.; Keblinski, P. Thermal transport across a substrate–thin-film interface: Effects of film thickness and surface roughness. *Phys. Rev. Lett.* **2014**, *113*, 65901. [\[CrossRef\]](#)
152. Vera, J.; Bayazitoglu, Y. Temperature and heat flux dependence of thermal resistance of water/metal nanoparticle interfaces at sub-boiling temperatures. *Int. J. Heat Mass Transf.* **2015**, *86*, 433–442. [\[CrossRef\]](#)
153. Pham, A.T.; Barisik, M.; Kim, B. Molecular dynamics simulations of Kapitza length for argon-silicon and water-silicon interfaces. *Int. J. Precis. Eng. Manuf.* **2014**, *15*, 323–329. [\[CrossRef\]](#)
154. Ong, Z.Y. Thickness-dependent Kapitza resistance in multilayered graphene and other two-dimensional crystals. *Phys. Rev. B* **2017**, *95*, 155309. [\[CrossRef\]](#)
155. Ghatage, D.; Tomar, G.; Shukla, R.K. Thermostat-induced spurious interfacial resistance in non-equilibrium molecular dynamics simulations of solid–liquid and solid–solid systems. *J. Chem. Phys.* **2020**, *153*, 164110. [\[CrossRef\]](#) [\[PubMed\]](#)
156. Pham, A.; Barisik, M.; Kim, B. Pressure dependence of Kapitza resistance at gold/water and silicon/water interfaces. *J. Chem. Phys.* **2013**, *139*, 244702. [\[CrossRef\]](#) [\[PubMed\]](#)
157. Amani, A.; Karimian, S.; Seyednia, M. A molecular dynamics simulation on the effect of different parameters on thermal resistance of graphene-argon interface. *Mol. Simul.* **2017**, *43*, 276–283. [\[CrossRef\]](#)
158. Vo, T.Q.; Kim, B. Interface thermal resistance between liquid water and various metallic surfaces. *Int. J. Precis. Eng. Manuf.* **2015**, *16*, 1341–1346. [\[CrossRef\]](#)
159. France-Lanord, A.; Soukiassian, P.; Glattli, C.; Wimmer, E. Ab initio parameterization of a charge optimized many-body forcefield for Si–SiO₂: Validation and thermal transport in nanostructures. *J. Chem. Phys.* **2016**, *144*, 104705. [\[CrossRef\]](#) [\[PubMed\]](#)
160. Ge, S.; Chen, M. Vibrational coupling and Kapitza resistance at a solid–liquid interface. *Int. J. Thermophys.* **2013**, *34*, 64–77. [\[CrossRef\]](#)
161. Murad, S.; Puri, I.K. Thermal transport across nanoscale solid-fluid interfaces. *Appl. Phys. Lett.* **2008**, *92*, 133105. [\[CrossRef\]](#)
162. Biolè, D.; Bertola, V. A goniometric mask to measure contact angles from digital images of liquid drops. *Colloids Surfaces Physicochem. Eng. Asp.* **2015**, *467*, 149–156. [\[CrossRef\]](#)
163. Biolè, D.; Wang, M.; Bertola, V. Assessment of direct image processing methods to measure the apparent contact angle of liquid drops. *Exp. Therm. Fluid Sci.* **2016**, *76*, 296–305. [\[CrossRef\]](#)
164. Wang, J.; Betelu, S.; Law, B. Line tension approaching a first-order wetting transition: Experimental results from contact angle measurements. *Phys. Rev. E* **2001**, *63*, 031601. [\[CrossRef\]](#)
165. Brinkmann, M.; Kierfeld, J.; Lipowsky, R. A general stability criterion for droplets on structured substrates. *J. Phys. Math. Gen.* **2004**, *37*, 11547. [\[CrossRef\]](#)
166. Barisik, M.; Beskok, A. Wetting characterisation of silicon (1, 0, 0) surface. *Mol. Simul.* **2013**, *39*, 700–709. [\[CrossRef\]](#)
167. Shi, Z.; Barisik, M.; Beskok, A. Molecular dynamics modeling of thermal resistance at argon-graphite and argon-silver interfaces. *Int. J. Therm. Sci.* **2012**, *59*, 29–37. [\[CrossRef\]](#)
168. Pompe, T.; Herminghaus, S. Three-phase contact line energetics from nanoscale liquid surface topographies. *Phys. Rev. Lett.* **2000**, *85*, 1930. [\[CrossRef\]](#) [\[PubMed\]](#)
169. Goicochea, J.V.; Hu, M.; Michel, B.; Poulikakos, D. Surface Functionalization Mechanisms of Enhancing Heat Transfer at Solid-Liquid Interfaces. *J. Heat Transf.* **2011**, *133*, ARTN-082401. [\[CrossRef\]](#)
170. Acharya, H.; Mozdierz, N.; Keblinski, P.; Garde, S. How Chemistry, Nanoscale Roughness, and the Direction of Heat Flow Affect Thermal Conductance of Solid-Water Interfaces. *Ind. Eng. Chem. Res.* **2012**, *51*, 1767–1773. [\[CrossRef\]](#)
171. Lundgren, M.; Allan, N.L.; Cosgrove, T. Modeling of wetting: A study of nanowetting at rough and heterogeneous surfaces. *Langmuir* **2007**, *23*, 1187–1194. [\[CrossRef\]](#)
172. Halverson, J.D.; Maldarelli, C.; Couzis, A.; Koplik, J. Atomistic simulations of the wetting behavior of nanodroplets of water on homogeneous and phase separated self-assembled monolayers. *Soft Matter* **2010**, *6*, 1297–1307. [\[CrossRef\]](#)
173. Israelachvili, J.N.; Gee, M.L. Contact angles on chemically heterogeneous surfaces. *Langmuir* **1989**, *5*, 288–289. [\[CrossRef\]](#)
174. Wang, J.; Bratko, D.; Luzar, A. Probing surface tension additivity on chemically heterogeneous surfaces by a molecular approach. *Proc. Natl. Acad. Sci. USA* **2011**, *108*, 6374–6379. [\[CrossRef\]](#) [\[PubMed\]](#)
175. Blander, M.; Katz, J.L. Bubble nucleation in liquids. *AIChE J.* **1975**, *21*, 833–848. [\[CrossRef\]](#)
176. Kelton, K.; Greer, A.L. *Nucleation in Condensed Matter: Applications in Materials And Biology*; Elsevier: Amsterdam, The Netherlands, 2010.
177. Zeng, X.; Oxtoby, D.W. Gas–liquid nucleation in Lennard-Jones fluids. *J. Chem. Phys.* **1991**, *94*, 4472–4478. [\[CrossRef\]](#)
178. Shen, V.K.; Debenedetti, P.G. Density-functional study of homogeneous bubble nucleation in the stretched Lennard-Jones fluid. *J. Chem. Phys.* **2001**, *114*, 4149–4159. [\[CrossRef\]](#)
179. Wilhelmsen, Ø.; Bedeaux, D.; Kjølstrup, S.; Reguera, D. Thermodynamic stability of nanosized multicomponent bubbles/droplets: The square gradient theory and the capillary approach. *J. Chem. Phys.* **2014**, *140*, 24704. [\[CrossRef\]](#) [\[PubMed\]](#)

180. Delale, C.F.; Hruby, J.; Marsik, F. Homogeneous bubble nucleation in liquids: The classical theory revisited. *J. Chem. Phys.* **2003**, *118*, 792–806. [\[CrossRef\]](#)
181. Shen, V.K.; Debenedetti, P.G. A kinetic theory of homogeneous bubble nucleation. *J. Chem. Phys.* **2003**, *118*, 768–783. [\[CrossRef\]](#)
182. Zhukhovitskii, D. Molecular dynamics study of cluster evolution in supersaturated vapor. *J. Chem. Phys.* **1995**, *103*, 9401–9407. [\[CrossRef\]](#)
183. Yasuoka, K.; Matsumoto, M. Molecular dynamics of homogeneous nucleation in the vapor phase. I. Lennard-Jones fluid. *J. Chem. Phys.* **1998**, *109*, 8451–8462. [\[CrossRef\]](#)
184. Yasuoka, K.; Matsumoto, M. Molecular dynamics of homogeneous nucleation in the vapor phase. II. Water. *J. Chem. Phys.* **1998**, *109*, 8463–8470. [\[CrossRef\]](#)
185. Maruyama, S.; Kimura, T.; Yamaguchi, Y. A molecular dynamics simulation of a bubble nucleation on solid surface. In *Proceedings of the National Heat Transfer Symposium of Japan*; Heat Transfer Society of Japan: Tokyo, Japan, 1997; Volume 34, pp. 675–676.
186. Kimura, T.; Maruyama, S. Molecular dynamics simulation of heterogeneous nucleation of a liquid droplet on a solid surface. *Microscale Thermophys. Eng.* **2002**, *6*, 3–13. [\[CrossRef\]](#)
187. Nagayama, G.; Cheng, P. Effects of interface wettability on microscale flow by molecular dynamics simulation. *Int. J. Heat Mass Transf.* **2004**, *47*, 501–513. [\[CrossRef\]](#)
188. She, X.; Shedd, T.A.; Lindeman, B.; Yin, Y.; Zhang, X. Bubble formation on solid surface with a cavity based on molecular dynamics simulation. *Int. J. Heat Mass Transf.* **2016**, *95*, 278–287. [\[CrossRef\]](#)
189. Davis, E.J.; Ray, A.K. Submicron droplet evaporation in the continuum and non-continuum regimes. *J. Aerosol Sci.* **1978**, *9*, 411–422. [\[CrossRef\]](#)
190. Little, J.K. *Simulation of Droplet Evaporation in Supercritical Environments Using Parallel Molecular Dynamics*; The Pennsylvania State University: State College, PA, USA, 1996.
191. Kuo, K.K. *Principles of Combustion*; Wiley: State College, PA, USA, 2005.
192. Walther, J.H.; Koumoutsakos, P. Molecular dynamics simulation of nanodroplet evaporation. *J. Heat Transf.* **2001**, *123*, 741–748. [\[CrossRef\]](#)
193. Gong, Y.; Xiao, G.; Ma, X.; Luo, K.H.; Shuai, S.; Xu, H. Phase transitions of multi-component fuel droplets under sub-and supercritical conditions. *Fuel* **2021**, *287*, 119516. [\[CrossRef\]](#)
194. Ju, D.; Huang, L.; Zhang, K.; Ye, M.; Huang, Z.; Yi, G. Comparison of evaporation rate constants of a single fuel droplet entering subcritical and supercritical environments. *J. Mol. Liq.* **2022**, *347*, 118346. [\[CrossRef\]](#)
195. Wu, Y.; Pan, C. Molecular dynamics simulation of thin film evaporation of Lennard-Jones liquid. *Nanoscale Microscale Thermophys. Eng.* **2006**, *10*, 157–170. [\[CrossRef\]](#)
196. Yi, P.; Poulikakos, D.; Walther, J.; Yadigaroglu, G. Molecular dynamics simulation of vaporization of an ultra-thin liquid argon layer on a surface. *Int. J. Heat Mass Transf.* **2002**, *45*, 2087–2100. [\[CrossRef\]](#)
197. Dou, Y.; Zhigilei, L.V.; Winograd, N.; Garrison, B.J. Explosive boiling of water films adjacent to heated surfaces: A microscopic description. *J. Phys. Chem. A* **2001**, *105*, 2748–2755. [\[CrossRef\]](#)
198. Li, C.; Wang, Z.; Wang, P.I.; Peles, Y.; Koratkar, N.; Peterson, G. Nanostructured copper interfaces for enhanced boiling. *Small* **2008**, *4*, 1084–1088. [\[CrossRef\]](#) [\[PubMed\]](#)
199. Chen, R.; Lu, M.C.; Srinivasan, V.; Wang, Z.; Cho, H.H.; Majumdar, A. Nanowires for enhanced boiling heat transfer. *Nano Lett.* **2009**, *9*, 548–553. [\[CrossRef\]](#)
200. Betz, A.R.; Xu, J.; Qiu, H.; Attinger, D. Do surfaces with mixed hydrophilic and hydrophobic areas enhance pool boiling? *Appl. Phys. Lett.* **2010**, *97*, 141909. [\[CrossRef\]](#)
201. Yao, Z.; Lu, Y.W.; Kandlikar, S. Effects of nanowire height on pool boiling performance of water on silicon chips. *Int. J. Therm. Sci.* **2011**, *50*, 2084–2090. [\[CrossRef\]](#)
202. Weibel, J.A.; Kim, S.; Fisher, T.S.; Garimella, S.V. Carbon nanotube coatings for enhanced capillary-fed boiling from porous microstructures. *Nanoscale Microscale Thermophys. Eng.* **2012**, *16*, 1–17. [\[CrossRef\]](#)
203. Kim, D.E.; Yu, D.I.; Jerng, D.W.; Kim, M.H.; Ahn, H.S. Review of boiling heat transfer enhancement on micro/nanostructured surfaces. *Exp. Therm. Fluid Sci.* **2015**, *66*, 173–196. [\[CrossRef\]](#)
204. Nagayama, G.; Tsuruta, T. A general expression for the condensation coefficient based on transition state theory and molecular dynamics simulation. *J. Chem. Phys.* **2003**, *118*, 1392–1399. [\[CrossRef\]](#)
205. Kesälä, E.; Kuronen, A.; Nordlund, K. Molecular dynamics simulation of pressure dependence of cluster growth in inert gas condensation. *Phys. Rev. B* **2007**, *75*, 174121. [\[CrossRef\]](#)
206. Ranathunga, D.T.; Shamir, A.; Dai, X.; Nielsen, S.O. Molecular dynamics simulations of water condensation on surfaces with tunable wettability. *Langmuir* **2020**, *36*, 7383–7391. [\[CrossRef\]](#) [\[PubMed\]](#)
207. Wang, T.; Liu, X.; He, M.; Zhang, Y. Molecular dynamics simulation of thermophysical properties and condensation process of R1233zd (E). *Int. J. Refrig.* **2020**, *112*, 341–347. [\[CrossRef\]](#)
208. Hinds, B.J.; Chopra, N.; Rantell, T.; Andrews, R.; Gavalas, V.; Bachas, L.G. Aligned multiwalled carbon nanotube membranes. *Science* **2004**, *303*, 62–65. [\[CrossRef\]](#) [\[PubMed\]](#)
209. Bernard, S.; Wirth, R.; Schreiber, A.; Schulz, H.M.; Horsfield, B. Formation of nanoporous pyrobitumen residues during maturation of the Barnett Shale (Fort Worth Basin). *Int. J. Coal Geol.* **2012**, *103*, 3–11. [\[CrossRef\]](#)

210. Park, S.; Kim, Y.S.; Kim, W.B.; Jon, S. Carbon nanosyringe array as a platform for intracellular delivery. *Nano Lett.* **2009**, *9*, 1325–1329. [\[CrossRef\]](#)
211. Travis, K.P.; Todd, B.; Evans, D.J. Departure from Navier-Stokes hydrodynamics in confined liquids. *Phys. Rev. E* **1997**, *55*, 4288. [\[CrossRef\]](#)
212. Travis, K.P.; Gubbins, K.E. Poiseuille flow of Lennard-Jones fluids in narrow slit pores. *J. Chem. Phys.* **2000**, *112*, 1984–1994. [\[CrossRef\]](#)
213. Koplik, J.; Banavar, J.R. Continuum deductions from molecular hydrodynamics. *Annu. Rev. Fluid Mech.* **1995**, *27*, 257–292. [\[CrossRef\]](#)
214. Zhang, C.; Chen, Y.; Yang, L.; Shi, M. Self-diffusion for Lennard-Jones fluid confined in a nanoscale space. *Int. J. Heat Mass Transf.* **2011**, *54*, 4770–4773. [\[CrossRef\]](#)
215. Sokhan, V.P.; Nicholson, D.; Quirke, N. Fluid flow in nanopores: Accurate boundary conditions for carbon nanotubes. *J. Chem. Phys.* **2002**, *117*, 8531–8539. [\[CrossRef\]](#)
216. Stokes, G. On the effect of the internal friction of fluids on the motion of pendulums. *Trans. Camb. Philos. Soc.* **1850**, *3*, 1880–1905.
217. Cao, B.Y.; Sun, J.; Chen, M.; Guo, Z.Y. Molecular momentum transport at fluid-solid interfaces in MEMS/NEMS: A review. *Int. J. Mol. Sci.* **2009**, *10*, 4638–4706. [\[CrossRef\]](#) [\[PubMed\]](#)
218. Wu, H.; Cheng, P. Friction factors in smooth trapezoidal silicon microchannels with different aspect ratios. *Int. J. Heat Mass Transf.* **2003**, *46*, 2519–2525. [\[CrossRef\]](#)
219. Soong, C.; Yen, T.; Tzeng, P. Molecular dynamics simulation of nanochannel flows with effects of wall lattice-fluid interactions. *Phys. Rev. E* **2007**, *76*, 036303. [\[CrossRef\]](#)
220. Gandomi, Y.A.; Edmundson, M.; Busby, F.; Mench, M.M. Water management in polymer electrolyte fuel cells through asymmetric thermal and mass transport engineering of the micro-porous layers. *J. Electrochem. Soc.* **2016**, *163*, F933. [\[CrossRef\]](#)
221. Ge, S.; Gu, Y.; Chen, M. A molecular dynamics simulation on the convective heat transfer in nanochannels. *Mol. Phys.* **2015**, *113*, 703–710. [\[CrossRef\]](#)
222. Shkarah, A.J.; Sulaiman, M.Y.B.; Ayob, M.R.B.H.; Togun, H. A 3D numerical study of heat transfer in a single-phase micro-channel heat sink using graphene, aluminum and silicon as substrates. *Int. Commun. Heat Mass Transf.* **2013**, *48*, 108–115. [\[CrossRef\]](#)
223. Thekkethala, J.F.; Sathian, S.P. The effect of graphene layers on interfacial thermal resistance in composite nanochannels with flow. *Microfluid. Nanofluid.* **2015**, *18*, 637–648. [\[CrossRef\]](#)
224. Ghasemi, H.; Ward, C. Mechanism of sessile water droplet evaporation: Kapitza resistance at the solid–liquid interface. *J. Phys. Chem. C* **2011**, *115*, 21311–21319. [\[CrossRef\]](#)
225. Marable, D.C.; Shin, S.; Nobakht, A.Y. Investigation into the microscopic mechanisms influencing convective heat transfer of water flow in graphene nanochannels. *Int. J. Heat Mass Transf.* **2017**, *109*, 28–39. [\[CrossRef\]](#)
226. Motlagh, M.B.; Kalteh, M. Molecular dynamics simulation of nanofluid convective heat transfer in a nanochannel: Effect of nanoparticles shape, aggregation and wall roughness. *J. Mol. Liq.* **2020**, *318*, 114028. [\[CrossRef\]](#)
227. Motlagh, M.B.; Kalteh, M. Simulating the convective heat transfer of nanofluid Poiseuille flow in a nanochannel by molecular dynamics method. *Int. Commun. Heat Mass Transf.* **2020**, *111*, 104478. [\[CrossRef\]](#)
228. Chakraborty, P.; Ma, T.; Cao, L.; Wang, Y. Significantly enhanced convective heat transfer through surface modification in nanochannels. *Int. J. Heat Mass Transf.* **2019**, *136*, 702–708. [\[CrossRef\]](#)
229. Toghraie, D.; Hekmatifar, M.; Salehipour, Y.; Afrand, M. Molecular dynamics simulation of Couette and Poiseuille Water-Copper nanofluid flows in rough and smooth nanochannels with different roughness configurations. *Chem. Phys.* **2019**, *527*, 110505. [\[CrossRef\]](#)
230. Jiang, L.; Wong, M.; Zohar, Y. Forced convection boiling in a microchannel heat sink. *J. Microelectromech. Syst.* **2001**, *10*, 80–87. [\[CrossRef\]](#)
231. Qu, W.; Mudawar, I. Flow boiling heat transfer in two-phase micro-channel heat sinks—II. Annular two-phase flow model. *Int. J. Heat Mass Transf.* **2003**, *46*, 2773–2784. [\[CrossRef\]](#)
232. Maruyama, S. Molecular dynamics method for microscale heat transfer. *Adv. Numer. Heat Transf.* **2000**, *2*, 189–226.
233. Qu, W.; Mudawar, I. Flow boiling heat transfer in two-phase micro-channel heat sinks—I. Experimental investigation and assessment of correlation methods. *Int. J. Heat Mass Transf.* **2003**, *46*, 2755–2771. [\[CrossRef\]](#)
234. Zarringhalam, M.; Ahmadi-Danesh-Ashtiani, H.; Toghraie, D.; Fazaeli, R. The effects of suspending Copper nanoparticles into Argon base fluid inside a microchannel under boiling flow condition by using of molecular dynamic simulation. *J. Mol. Liq.* **2019**, *293*, 111474. [\[CrossRef\]](#)

Disclaimer/Publisher’s Note: The statements, opinions and data contained in all publications are solely those of the individual author(s) and contributor(s) and not of MDPI and/or the editor(s). MDPI and/or the editor(s) disclaim responsibility for any injury to people or property resulting from any ideas, methods, instructions or products referred to in the content.